Reelin cells and sex-dependent synaptopathology in autism following postnatal immune activation

Maryam Ardalan[1,2], Tetyana Chumak[1], Alexandra Quist[1], Eva Hermans[1,5], Ali Hoseinpoor Rafati[2], Giacomo Gravina[1], Seyedeh Marziyeh Jabbari Shiadeh[2], Pernilla Svedin[1], Setareh Alabaf[1], Brian Hansen [4], Gregers Wegener[2], Lars Westberg[3], Carina Mallard[1]

[1]Department of Physiology, Institute of Neuroscience and Physiology, Sahlgrenska Academy, University of Gothenburg, Gothenburg, Sweden

[2]Department of Clinical Medicine, Translational Neuropsychiatry Unit, Aarhus University, Aarhus, Denmark

[3]Department of Pharmacology, Institute of Neuroscience and Physiology, Sahlgrenska Academy, University of Gothenburg, Gothenburg, Sweden

[4]Department of Clinical Medicine, Center of Functionally Integrative Neuroscience-SKS, Aarhus University, Aarhus, Denmark

[5]Department of Developmental Origins of Disease, Utrecht Brain Center and Wilhelmina Children's Hospital, Utrecht University, Utrecht, Netherland

Corresponding author:

Carina Mallard, PhD, Professor, Department of Physiology, Institute of Neuroscience and Physiology, Sahlgrenska Academy, University of Gothenburg, Box 432, SE-405 30 Gothenburg, Sweden, Phone: +46 705-631004; Email: carina.mallard@neuro.gu.se

Running title: Reelin and neonatal inflammation and autism

Abstract

Autism Spectrum Disorders (ASD) are heterogeneous neurodevelopmental disorders with considerably increased risk in male infants born preterm and with neonatal infection. Here we investigated the role of postnatal immune activation on hippocampal synaptopathology by targeting Reelin+ cells in mice with ASD-like behavior.

C57/Bl6 mouse pups of both sexes received lipopolysaccharide (LPS, 1mg/kg) on postnatal day (P) 5. At P45, animal behavior was examined by marble burying and sociability test, followed by ex-vivo brain MRI diffusion kurtosis imaging (DKI). Hippocampal synaptogenesis, number and morphology of Reelin+ cells, and mRNA expression of trans-synaptic genes, including neurexin-3, neuroligin-1, and cell-adhesion molecule nectin-1 were analyzed at P12 and P45.

Social withdrawal and increased stereotypic activities in males were related to increased mean diffusivity on MRI-DKI and overgrowth in hippocampus together with retention of long-thin immature synapses on apical dendrites, decreased volume and number of Reelin+ cells as well as reduced expression of trans-synaptic and cell-adhesion molecules.

The study provides new insights into sex-dependent mechanisms that may underlie ASD-like behavior in males following PIA. We identify GABAergic interneurons as core components of dysmaturation of excitatory synapses in the hippocampus following postnatal infection and provide cellular and molecular substrates for the MRI findings with translational value.

Keywords: Autism, preterm, neonatal infection, synaptogenesis, Reelin, MRI diffusion kurtosis

Introduction

Preterm birth and its associated complications are among the most serious global health issues that modern society faces (1, 2). Particularly, extreme prematurity (<28 gestational weeks) is associated with a substantially elevated risk of neurodevelopmental problems, including up to 41% for autistic spectrum disorders (ASD) (3-5). A recent large network study in the USA showed that the prevalence of ASD is significantly higher in boys (23.4 per 1,000) than girls (5.2 per 1,000) (6). There are also distinct sex-dependent phenotypic characteristics showing that autistic females have significantly lower internalizing and anxiety problems than ASD males (7, 8). Identifying pathophysiological and behavioral differences between males and females with autism is crucial for understanding the etiology and may help in the early diagnosis of autism (9).

Besides a strong genetic component underlying ASD, environmental factors are important (10, 11). It was suggested that the combination of preterm birth and susceptibility genes makes infants more vulnerable to environmental factors such as infection after birth and contribute to autism pathogenesis (12). In support of the inflammation hypothesis, blood monocytes from children with ASD demonstrate distinct cytokine responses following activation of the innate immune system (13). Postnatal immune activation (PIA) by lipopolysaccharide (LPS), a toll-like receptor (TLR- 4) agonist which mimics Gram-negative bacterial infection (14), leads to ASD-like behavior in animals (15). While inflammation and prematurity have emerged as joint driving forces in ASD, due to the heterogeneous nature of autism, conclusive evidence for etiology and pathogenesis has yet to be established. Individuals with ASD show overgrowth of brain regions, such as cornu ammonis sectors (CA) 1–3 of the hippocampus, already at six months of age suggesting that ASD manifests at an early age (16).

Alterations in neuronal plasticity has been implicated in ASD neuropathology. Of particular relevance for the regulation of neuronal plasticity is genes encoding trans-synaptic adhesion proteins, including presynaptic neurexins (NRXNs), postsynaptic neuroligins (NLGNs) and cellular adhesion molecules, including Nectin-1 (17). These proteins affect various aspects of synapse biology, including synaptogenesis, synaptic transmission, remodeling and maturation (18, 19). NRXN3 and NLGN1 mutations have been associated with ASD (20-23) by regulating differentiation of excitatory and inhibitory synapses (24). Importantly, Nectin-1 regulates dendritic spine density and inhibition of Nectin-1 results in increased number of synapses in the hippocampus (25, 26). Reelin, an extracellular matrix protein expressed by a population of GABAergic Cajal Retzius (CR) interneurons, is essential for synaptic plasticity through affecting dendrites and dendritic spine development. Reelin-signaling regulates pre-and postsynaptic structure/function by impinging trans-synaptic adhesion proteins such as NLGN, NRXN and Nectin-1. Deficits in brain levels of reelin mRNA were reported in ASD cases and it has been studied as a potential biomarker for autism (27). Despite the importance of reelin-

signaling in synapse plasticity and ASD, it is unknown how adverse early life experience such as PIA affects these pathways and how it is related to sex-dependent autistic-like behaviors. Therefore, this study aimed to explore sex-dependent effects of PIA on microstructure MRI parameters, Reelin+ cells and trans-synaptic adhesion proteins in connection with synapse plasticity in the hippocampus in an animal model of postnatal infection with ASD-like phenotype. Importantly, we investigated neuropathological changes at early pediatric age and later in adolescent age to evaluate the impact of PIA on brain development over time.

Material and methods

Materials:

C57Bl/6J wild-type (WT) mice were purchased from Janvier Labs (Le Genest-Saint-Isle, France) and Charles River Laboratories (Sulzfeld, Germany) and fed standard laboratory chow diet (B&K, Solna, Sweden); Lipopolysaccharide (LPS, #423, List Biological Laboratories, Campbell, CA, USA); Saline (Sigma Aldrich, St. Louis, MO, USA); Pentobarbital (Pentacour UK); 6% buffered formaldehyde (Histofix; Histolab products AB, Västra Frölunda, Sweden); Isopentane (Sigma Aldrich, USA); Cryostat (Leica, CM 3050 S, Germany); FD Rapid Golgi Stain TM Kit (FD Neuro Technologies, Inc., Columbia, MD, USA); Vibratome (Leica, VT1200S Semiautomatic Vibrating Blade Microtome, Wetzlar, Germany); Thionin solution (Sigma T3387, USA); Phosphate-buffered saline (Gibco Invitrogen, Waltham, MA, USA); Target retrieval solution (Dako, Glostrup, Denmark); 0.02% Triton-X-100 (PBS-T, Sigma Aldrich, USA); rabbit anti-Iba1 (019-19741, Wako, Japan); anti-reelin (ab78540, RRID:AB_1603148); goat-anti-rabbit antibody (Vector Laboratories, Olean, NY, USA); ABC elite solution (Vector Laboratories, USA); 3,30-diaminobenzidine solution (Acros Organics, Geel, Belgium); gelatin-coated slides (Sigma Aldrich, USA), Digital camera (Leica DFC 295, Germany); newCAST™ software (Visopharm, Hørsholm, Denmark); Nanodrop (2000/2000c, Thermo Scientific, Rockford, IL, USA); QuantiTect Reverse Transcription Kit (Qiagen, USA). Quanti Fast SYBR Green PCR Master Mix (Qiagen, USA); PCR primers (Qiagen, USA), LightCycler 480 (Roche, Sweden). Quant-IT OliGreen ssDNA Assay kit (Fisher Scientific, Sweden).

Animals and induction of postnatal immune activation (PIA)

C57Bl/6J wild-type (WT) mice were purchased from Janvier Labs (Le Genest-Saint-Isle, France) and Charles River Laboratories (Sulzfeld, Germany) and were bred in the animal facility at the University of Gothenburg (Experimental Biomedicine, University of Gothenburg). Mice were housed with a normal 12-h light/dark cycle (lights on at 06:00) and ad libitum access to standard laboratory chow diet (B&K, Solna, Sweden) and drinking water in a temperature-controlled environment (20–22°C). All animal experiments were approved by the Gothenburg Animal Ethical Committee (No 663/2017 with amendment Dnr 5.8.18-14322/2018). Mice of

both sexes were used. Sex was established by visual inspection. In each experimental group, mice were obtained from at least three different litters. Postnatal immune activation (PIA) was induced in male and female mice by a single intraperitoneal injection of lipopolysaccharide (LPS) (1mg/kg, #423, List Biological Laboratories, Campbell, CA, USA), a well-established animal model in postnatal day (P) 5 mice for studying effects of peripheral inflammation on brain function (28). This age in mice represents a critical brain developmental stage equivalent to preterm human infants (29). Control animals received an equal volume of saline (Sigma Aldrich, St. Louis, MO, USA). The experiments included two follow up time points: 7 days after injection (P12) and 40±5 days after injection (P45±5), corresponding to pediatric and adolescent age respectively. Accordingly, there were eight groups, with equal number of male and female mice in each group, for each parameter studied. After weaning (P23), the mice were separated based on sex and kept in standard conditions in the animal house (5 mice from the same sex in each cage).

Behavioral Tests

Male and female mice were evaluated at P45±5 (n = 10/treatment group/sex) for stereotypic and repetitive behavior (marble burying test), sociability and interest in social novelty (three-chamber test). Before the initiation of behavioral tests mice were allowed to acclimatize to the test room for one hour. For each mouse, behavioral tests were performed at the same time every day (9 am - 4 pm) at 60 lux illumination level, starting with the marble-burying test followed by the three-chamber with a resting time of 30 min between tests. Four mice from the same sex were tested per day. Test chamber and marbles were cleaned with 70% alcohol between each mouse.

Marble burying test: The test was performed according to the Deacon protocol (30). Briefly, 20 glass marbles (1.5 cm in diameter) were placed on the top of the bedding (in 5 rows of 4 marbles) in a Plexiglas box (32 cm (length) × 30 cm (width) × 18 cm (height)) with 5 cm bedding. Each mouse was placed in the box for 30 min and at the end of the test, the number of buried marbles was counted. The criteria to count marbles as buried was that they were at least covered to 50% by bedding.

Three-chamber test: Mouse sociability was examined as previously described (31) with minor modifications. Briefly, a stimulus mouse (sex- and age-matched with no previous contact with the test mouse) was selected from a separately reared cage. The stimulus mouse was habituated by being placed inside a pencil cup for 30 min once per day for 2 days prior to the beginning of the test. On the day of testing, both the stimulus and the test mouse were habituated to the testing room for 1 h prior to the start of behavioral tasks. The size of the chambers were: middle (25 cm height × 18.7 cm width), chamber 1 (25 cm height × 19.5 cm width) and chamber 2 (25 cm height × 19.5 cm width) with the overall dimensions of the box

being: 25 cm (height) × 44 cm (width) ×59 cm (length). Between the chambers there was a 1 cm wide gap which could be closed or opened during testing. The size of the pencil cup was 10 cm in height with a diameter of 8.4 cm at the bottom. The following test procedure was employed: 1) the test mouse was placed for 10 min in the middle chamber with closed gaps (habituation step); 2) the gaps between chambers were opened and the test mouse allowed to explore all three chambers freely for 10 min (exploration step); 3) the stimulus mouse was placed inside an empty pencil cup in one of the chambers, and in the other chamber an identical empty pencil cup was placed and the test mouse was allowed to freely explore all three chambers for 10 min; 4) the test mouse was returned to its resting cage. For the test mouse, the following parameters were scored by a blinded researcher: 1) time spent in empty pencil cup chamber and 2) time spent in the stimulus mouse chamber. Quantification of social behaviours was performed manually by a researcher blinded to the groups of test mice. The sociability index (SI) was calculated as: (time exploring social chamber-time exploring non-social chamber)/(time exploring social chamber + time exploring non-social chamber) as described (32).

Tissue processing for histological, immunohistochemical and Golgi staining

At P12 (n = 6/treatment group/sex) and P45±5 (n = 8/treatment group/sex) mice were deeply anaesthetized via intraperitoneal administration of pentobarbital (Pentacour, 60 mg/ml). Animals at P45 were randomly selected from behavioral groups 30 min after completion of tests. The brains were removed from the skull and the right or left hemisphere was selected randomly, immersed in 6% buffered formaldehyde (Histofix; Histolab products AB, Västra Frölunda, Sweden) and stored at 4 °C until further processing. At the time of tissue processing, hemispheres were placed in a cryoprotective solution containing 30% ($w.v^{-1}$) sucrose for 48 h followed by placement on copper blocks for freezing in cold isopentane (Sigma Aldrich). Free floating 40-µm thick brain sections were cut coronally on a cryostat (Leica, CM 3050 S, Germany) including the hippocampus (bregma -0.94 mm to -4.20 mm). Five series of sections were collected based on a systematic sampling principle and a section-sampling fraction of 1/8 (33) by selecting the first section of each series randomly using a random table. Therefore, each series included 8–10 sections with a fixed distance of 320 µm (8 × 40 µm).

The contralateral hemisphere was processed for rapid Golgi-Cox staining for impregnation of individual pyramidal neurons in the hippocampus using the FD Rapid Golgi Stain TM Kit (FD Neuro Technologies, Inc., Columbia, MD) following the manufacturer's instructions as described before (34). Briefly, Golgi-stained hemispheres were sliced coronally (section thickness: 170 µm for P45 and 150 µm for P12) on a vibratome (Leica, VT1200S Semiautomatic Vibrating Blade Microtome, Wetzlar, Germany) and mounted on gelatin-coated slides.

Systematic sampling ensured that the distribution of left and right hemispheres was equal between the groups.

Histological and immunohistochemical staining

One set of sections was Nissl stained with a 0.25% thionin solution (Sigma T3387) for determination of the volume of hippocampal subregions under light microscopy.

The rest of the series were labelled using primary antibodies for three-dimensional (3D) quantification of Reelin+ cells and 3D reconstruction of ionized calcium binding adaptor molecule 1 (Iba1)+ microglia. Briefly, free-floating 40 µm thick sections were washed in phosphate-buffered saline (PBS, Gibco Invitrogen, Waltham, MA, USA) for 20 min. Sections were incubated in target retrieval solution (Dako, Glostrup, Denmark) at 85°C for 40 min for antigen retrieval. Afterwards, sections were washed for 20 min in PBS, followed by blocking of endogenous peroxidases (3% H_2O_2 in PBS, Sigma Aldrich) for 10 min. Thereafter, sections were washed with PBS containing 0.02% Triton-X-100 (PBS-T, Sigma Aldrich) and then incubated with rabbit anti-Iba1 (1:1000, 019-19741, Wako) and mouse monoclonal anti-reelin (1:1500, ab78540) overnight at 4°C. The next day, sections were washed in PBS-T and subsequently incubated in polyclonal secondary biotinylated goat-anti-rabbit antibody (1:250, Vector Laboratories, Olean, NY, USA) in PBS-T for 2 h in room temperature (RT). Sections were washed in PBS-T followed by incubation in ABC elite solution (1.5% solution A + 1.5% solution B in PBS, Vector Laboratories) for 1 h at room temperature. Afterwards, sections were washed in PBS-T for 20 min and immunolabeling was performed by using 3,30-diaminobenzidine solution (Acros Organics, Geel, Belgium). Sections were washed in distilled water and stored in PBS. Finally, sections were mounted on gelatin-coated slides (1.3%, Sigma Aldrich), dehydrated through a graded series of alcohol (70%, 96%, 99%), cleared in xylene for 10 min and coverslipped.

Image acquisition of neurons, neuronal dendritic spine reconstruction and analysis

In Golgi-stained sections, six pyramidal neurons (six apical and six basal dendrites) per mouse were selected from the CA1 subregion for morphological analysis. Three-D capturing of neuronal images was performed using a light microscope modified for stereology with a digital camera (Leica DFC 295, Germany) and newCAST™ software (Visopharm, Hørsholm, Denmark). Pyramidal neurons were identified by their triangular-shaped soma from which apical dendrites and basal dendrites protrude. Selection criteria for sampling by the optical disector were: 1) neurons were completely separated from other cells, 2) all dendrites were intact and 3) the soma of the neuron was in the middle of the thickness of the section. Using a 63× oil-immersed lens, z-stacks of images were captured with a z-plane step size of 1 µm. The 3D analysis of reconstructed neurons including dendritic spines was performed using

Filament Tracer algorithm of the Imaris software (version 8.4, Bitplane A.G., Zurich, Switzerland) (34). For 3D reconstruction, the longest diameter of the cell body was used as a starting point. Branch endpoints and bifurcations were then manually selected through which branches and dendrites were traced. Morphological neuronal parameters were: 1) apical/basal dendrite length, 2) number of apical/basal dendritic terminals, 3) convex hull volume and 4) sholl analysis to estimate the complexity of the dendritic arborization. The analysis performed was based on regularly spaced concentric circles centered on the neuronal soma. The sum of the number of intersecting dendrites for all circles was quantified for each neuron in intervals of 20 µm (34, 35).

In addition to the neuronal morphology, general morphological spine parameters were determined: 1) number of spines on apical/basal dendrites 2), mean spine density (spines/10 µm), 3) spine area, 4) spine length, 5) spine neck length, 6) spine diameter and 7) spine neck diameter (36). Dendritic spines were also classified into three morphological subtypes using the automated Imaris spine classification analysis: 1) stubby spines with a length less than 1 µm, lacking a spine head and with an apparent neck, 2) mushroom spines with a length less than 3 µm and characterized by a short neck and large spine head and 3) long-thin spines with mean width of head ≥ mean width of neck and with elongated spine necks. General morphological parameters were calculated also for the different spine types.

Image acquisition, 3D reconstruction and analysis of microglia

A total of 10 Iba1 positive microglia in the hippocampal CA1.SR area was selected in each animal at P12 and P45 (n = 6/treatment group/sex) for 3D reconstruction and morphological analysis. Selection criteria for microglia were 1) cell bodies must be in the middle of the section thickness with a clear border, 2) all branches are intact, 3) branches of the cell should be easily distinguishable from other cells or background staining. A systematic set of Z-stacks of images and z-plane step size of 1µm by selecting the middle of section as zero was obtained on Iba1 stained sections by using a 63× oil-immersed lens on a light microscope modified for stereology. This acquisition procedure ensured capturing more than one microglia per image (37). The captured images were analyzed using Filament Tracers algorithm in the Imaris software. Morphological parameters were: 1) number of the cellular branches, 2) total length of the branches, and 3) sholl analysis based on the radial distance from the center of the microglia soma in 5 µm.

Estimation of total number of Reelin+ cells

At P12 and P45, unbiased counting of number of Reelin+ cells were performed in the CA1 subregion of hippocampus using 63× oil-immersed lens and applying the optical fractionator method (38). Delineation of the CA1 area was based on differentiating the CA1 pyramidal cell

layer from the CA2/CA3 pyramidal cell layer (subregion with larger dense packed cells compared with CA1) and the subiculum (the area with smaller cell number density and bigger pyramidal cell size compared with pyramidal cells found in CA1) with a 5× objective lens. To eliminate the effect of shrinkage of tissue sections due to tissue preparation, the optimal disector height was calculated from a pilot study where cells were counted through the full thickness of 8 selected hippocampal sections (systematic random sampling of sections between animals). The z-position of each counted Reelin+ cell and the section thickness per sampling frame were measured. Z-plot (histogram) of the counted cells indicated constant cell density in the thickness from 5 µm to 25 µm which corresponded to full penetration and linear shrinkage of the section in the thickness of 20 µm. The criterion for counting was that the cell soma was in focus and fully or partially in the unbiased counting frame without touching the forbidden lines. The following formula was used to calculate the total number of cells (39):

$$N = \frac{1}{SSF} \cdot \frac{1}{ASF} \cdot \frac{1}{HSF} \cdot \Sigma Q^{-}$$

N is the total number of Reelin+ neurons in CA1 area; ΣQ− is the number of counted cells; SSF is the section sampling fraction (1/8); ASF is an area sampling fraction; and HSF is the height sampling fraction (mean of the Q^{-}-weighted height of the disector).

Morphological analysis of Reelin+ cells

Reelin+ cells can be divided into subgroups based on cell size (small vs. large soma-dendritic-axonal arborizations) (40). Therefore, we measured the Reelin+ cell soma in the CA1 subregion of hippocampus at P12 and P45 by applying spatial rotator estimator independent of tissue orientation (41). The cell volume estimation was performed with a 100× oil-immersion objective lens by using a virtual 3D probe and making 6 intersection points between cell boundaries and test rays in a series of parallel focal planes with a good resolution. We sampled randomly 50-80 cells of each cell per animal by the optical disector with a height of 20 µm.

$$l_i^2 = \sum_k l_{ik}^2 \cdot (-1)^{k+1}$$

$$\hat{V} = d\pi \sum_{i=1}^{n} \ell_i^2.$$

Quantification of hippocampal subregion volumes on histological sections

The volume of the whole hippocampus and hippocampal subfields (granular cell layer (GCL) and CA1 striatum radiatum (CA1.SR)) were estimated on Nissl-stained sections by using the Cavalieri estimator (42) using a 10× objective lens under light microscope. Of note, volume

measurement of hippocampal subregions on the cryostat sections has the advantages of the negligible amount of shrinkage in the x- and y-axis. The used formula for determining the volume of the subregions was:

$$V = \Sigma P \cdot \left(\frac{a}{p}\right) \cdot T \cdot \frac{1}{SSF}$$

Where *ΣP* is the total number of the points hitting the region of interest per animal, *(a/p)* is the area per test point; *T* is the section thickness (40 µm) and *SSF* is the section sampling fraction (1/8).

Magnetic Resonance Imaging

Sample Preparation: Mice at P45 (n = 5/ treatment group/sex) were perfusion-fixed with heparin (10 $U \cdot mL^{-1}$)-treated 0.9% saline (pH = 7.3) for 2 min, followed by ice-cold 6% buffered formaldehyde (pH = 7.2–7.4) for 2 min. Following fixation, the head was separated from the body just below the skull base. The skin was then removed from the head to avoid susceptibility artifacts in the MRI due to air bubbles trapped in the fur during imaging. This in-skull brain preparation was previously used (43) and has the advantage of avoiding deformation of the brain.

Data Collection: MRI was performed using a 9.4T preclinical MRI system equipped with a bore-mounted 25 mm quadrature coil used for both excitation and reception. Prior to imaging, samples were washed for at least 24 hours in phosphate buffered saline (PBS, Sigma USA, P4417-50TAB) to increase signal by removal of excess fixative. The sample was then securely placed in a tube filled with fluorinert (FC-770, 3M inc.), which was fitted into the coil in such a manner that all sample vibration was avoided. High resolution B0-mapping was employed to ensure good shim conditions (particularly important for the DKI data collection).

Volumetric data was acquired at an in-plane resolution of 64 µm × 64 µm and a slice thickness of 200 µm using a RARE sequence. Scan details were effective echo time, TE=10 ms, repetition time (TR) = 3133 ms, 4 averages, RARE factor = 2. Total scan time was 23 min. After acquisition, data was inspected for artifacts and exported in the dicom format for volumetric processing. DKI data was acquired at 200 µm isotropic resolution using a segmented diffusion weighted echo planar imaging (EPI) sequence. Five unweighted images were acquired in each slice for normalization along with 20 encoding directions at each of 4 b-values (0, 0.8, 1.8, 2.0 ms/μm^2). Diffusion timings were δ/Δ = 7/16 ms, and remaining parameters were 5 avs, TE=30.27 ms, TR = 3000 ms, BW= 277 kHz, 80 axial slices.

DKI analysis: Diffusion kurtosis imaging (DKI) is an advanced neuroimaging modality which is an extension of diffusion tensor imaging by estimating the kurtosis (skewed distribution) of water diffusion based on a probability distribution function. DKI data was imported in Matlab (Mathworks Inc, USA) and preprocessed as described previously. Briefly, data was Rician

noise floor adjusted (44), denoised and corrected for Gibbs-ringing (45). Following a normalization step the data was fitted to the DKI signal equation using non-linear optimization (Matlab, The Mathworks, USA) as in (44). From the DKI fit the mean diffusivity (MD) and mean kurtosis (MK) were calculated for each sample (45, 46). Hippocampus was then delineated on the unweighted diffusion images for each sample. These delineations were used to extract average hippocampal MD and MK values for each sample. At this point blinding was lifted and the groups were tested for statistical differences in HC MD and MK using Matlab's two-sample Kolmogorov-Smirnov test.

Volumetric analysis from MRI images: The whole brain and hippocampi were delineated in the RARE MRI data using ITK-snap (47). From these delineations, the brain and hippocampi volumes were calculated as the product of the total brain and total hippocampal voxel count and the nominal MRI voxel volume.

Quantitative reverse transcription PCR

At P12 and P45 (n = 10/treatment group/sex), mice were deeply anaesthetized via intraperitoneal administration of pentobarbital (Pentacour) and the right and left hippocampi were rapidly dissected and stored at -80°C until analysis. Total mRNA was isolated from the hippocampus using the miRNeasy mini kit (Qiagen Inc.) according to the manufacturer's recommendations. Total RNA concentration and purity were measured by a Nanodrop (Thermo Scientific) at 235-, 260- and 280-nm. cDNA was prepared from 1ug RNA in a 20 µL reaction using QuantiTect Reverse Transcription Kit (Qiagen). Each PCR (20 µL), contained 2µL cDNA (12ng), 10µL Quanti Fast SYBR Green PCR Master Mix (Qiagen) and 2µL PCR primer (QuantiTech Primer Assay, Qiagen), were run on a LightCycler 480 (Roche, Sweden). The following primers were used Nlgn1 QuantiTech Primer Assay (QT00167580), Nrxn3 QuantiTech Primer Assay (QT00166621) and Pvrl1 (nectin-1) QuantiTech Primer Assay (QT00171703) all from Qiagen. Melting curve analysis was performed to ensure that only one PCR product was obtained. For quantification and for estimation amplification efficiency, a standard curve was generated using increasing concentrations of cDNA. The amplified transcripts were quantified with the relative standard curve and normalized by the cDNA concentration using the Quant-IT OliGreen ssDNA Assay kit (Fisher Scientific).

Statistical Analysis

All data were analyzed using SPSS (IBM Corp. Released 2013, Version 24.0. Armonk, NY, United States). Graphs were created using Prism 8 (GraphPad Software Inc., USA). Prior to statistical tests, normal distribution of data was checked by making a Q–Q plot of the data. The variance homogeneity of data was also examined by Levene's test. If the distribution of data was not normal, a logarithmic transformation was employed before statistical testing. For

the three-chamber test, repeated measures analysis of variance (ANOVA) was used to compare time spent in the chamber containing the stimulus mouse and time spent in the chamber containing the empty pencil cup. Continuous morphological, molecular data and sociability index were compared using two-way ANOVA followed by Tukey's post hoc test (equal variances) and Games-Howel (not equal variances) with adjusted *p* values. DKI data analysis was performed in MATLAB (Mathworks Inc, USA) as described previously (45). The mean values from six neurons and ten microglia of each animal in the morphological studies were treated as a single measurement in the data analysis. In all cases, the significance level was assumed at $p < 0.05$. The results are presented as mean ± standard deviation.

Results

PIA induces brain overgrowth and impairs fiber integrity in male adolescent mice

A feature in children with autism is increased brain volumes (48). As such, we performed volume measurements of the whole brain (excluding olfactory bulb and cerebellum) (Fig 1A, C) and entire hippocampi (Fig 1B, D) from MRI images at P45. The MRI analysis of brain volume revealed significant main effect of sex with significant LPS × sex interaction respectively ($F_{(1,19)}$= 23.420, p=0.000; $F_{(1,19)}$= 8.474, p=0.010). Games-Howell post hoc analysis revealed that LPS significantly increased the volume of brain in male mice (p=0.000) without significant effect in female mice (p=0.845, Fig 1C). Moreover, the MRI analysis showed significant main effect of sex and interaction with LPS treatment on the volume of hippocampi in males ($F_{(1,19)}$= 4.855, p=0.043; $F_{(1,19)}$= 7.769, p=0.013). Tukey post-hoc analysis revealed a significantly larger size of hippocampi in male LPS group compared with male saline mice (p=0.019) without significant effect in female LPS mice (p=0.935, Fig 1D). Partial Eta square η^2 for the effect of sex and treatment on the whole brain volume were 0.59 and 0.09 which indicated large and medium effects of sex and LPS treatment, while partial Eta square η^2 for the effect of sex and treatment on the hippocampi volume were 0.23 and 0.19, indicating large effects of both sex and LPS treatment on the hippocampi volume.

The volume measurement of hippocampal subregions on Nissl stained sections showed significant main effects of sex and LPS treatment on the volume of CA1.SR subregion of hippocampus respectively ($F_{(1,29)}$= 26.335, p=0.000; $F_{(1,29)}$= 19.035, p=0.000) without significant effect on the volume of GCL area (Fig 1E). Tukey post hoc analysis indicated that the volume of CA1.SR area was significantly larger in male LPS mice versus male saline group (p=0.001) without significant changes in female LPS group (p=0.364, Fig 1F). Partial Eta square η^2 for the effect of sex and treatment were 0.50 and 0.42 which indicated large effect of sex and LPS treatment on the volume of CA1.SR area. Based on these findings, all further morphological analyses were performed in the CA1.SR region of the hippocampus.

DKI, an emerging increasingly used technique that provides complementary information to traditional diffusion techniques on the complexity of the microstructure (49), revealed a shift towards higher mean diffusivity values (MD) in dorsal and ventral hippocampus in adolescent males after LPS as seen in the MD probability distributions (Fig 2A, B). In contrast, MD values were lower in female LPS mice compared with saline female animals (Fig 2A, C). There were no significant changes in mean kurtosis (MK) in either males or females after LPS (p>0.05, Fig 2D, E) although a tendency to lower MK values was seen in all LPS animals.

PIA alters microglia response at P12 and P45 independent of sex

To determine the microglia response following PIA connected with autism, we performed a detailed analysis of 3D branching pattern in reconstructed Iba1+ cells in the CA1.SR subregion of the hippocampus in saline (Fig 3D) and LPS (Fig 3H) treated mice.

At P12 there was a significant effect of LPS × sex on the length and number of microglia processes ($F_{(1,20)}$= 8.368, p=0.009; $F_{(1,20)}$= 6.048, p=0.023) respectively, with the main effects of sex ($F_{(1,20)}$= 5.841, p=0.025; $F_{(1,20)}$= 9.736, p=0.005) and LPS treatment ($F_{(1,20)}$= 51.815, p=0.000; $F_{(1,20)}$= 42.105, p=0.000). At baseline, the length and number of microglia process were significantly shorter and with fewer number of processes in female saline compared to the male saline groups (p=0.006, p=0.004, Fig 3A,B). Microglia processes were significantly shorter and fewer in male LPS compared to male saline mice (p=0.000, p=0.000) and in female LPS compared to saline female group (p=0.03, p=0.045, Fig 3 A, B). Moreover, Sholl analysis showed that the number of process intersections at 10 µm - 40 µm away from the cell soma were significantly lower in male LPS mice than male saline group (p<0.05), while in female mice, the complexity of microglia processes was only affected by LPS, 20 µm away from cell soma (p=0.033, Fig 3C).

At P45, there were significant main effects of sex ($F_{(1,20)}$= 5.969, p=0.024) and LPS treatment ($F_{(1,20)}$= 63.534, p=0.000) with the partial Eta square η^2 of 0.23 and 0.76 on the length of microglia processes and a significant effect of LPS treatment on number of microglia branches ($F_{(1,20)}$= 45.518, p=0.000), with the Eta square η^2 of 0.69, was observed (Fig 3E, F). At baseline, the length and number of microglia processes were not different between male and female saline groups (p=0.194, p=0.333, Fig 3E, F). Sholl analysis showed that the complexity of microglia processes (intersections at 5 µm - 45 µm away from the cell soma) in male LPS mice were significantly lower compared to the male saline group (p<0.05), while in LPS compared to saline female mice, the complexity of microglia processes was affected at 10 µm-30 µm away from cell soma (p<0.05, Fig 3G).

Sex-specific difference in autistic behavioral phenotypes following PIA

Repetitive behavior and impairment in sociability are core symptoms of autism. The marble burying test showed a significant main effect of LPS ($F_{(1, 39)}$ =41.25, p=0.000) and post-hoc analysis revealed that male and female offspring displayed increased repetitive behavior after LPS exposure respectively (p=0.000, p=0.004, Fig 4A). No significant difference between male and female saline groups was observed (p=0.947). Partial Eta square η2 for the effect treatment was 0.53, which indicated a large effect of LPS treatment on the number of buried marbles as a repetitive behavior.

In the three-chamber social interaction test, comparison between time spent in the chamber containing the stimulus (novel) mouse and time spent in the chamber containing the empty pencil cup showed that male saline mice spent significantly more time in the stimulus mouse chamber (p=0.006, Fig 4B), while male LPS group spent significantly less time in the novel mouse chamber (p=0.050, Fig 4B). The female LPS group did not show preference to any of two chambers (p=0.330, Fig 4B). The results also showed a significant main effect of LPS on sociability index (SI) with significant LPS × sex interaction respectively ($F_{(1,39)}$= 11.55, p=0.002; $F_{(1,39)}$= 7.33, p=0.01) and post-hoc analysis revealed that LPS reduced SI only in male offspring (p=0.012, Fig 4C).

PIA does not affect branching patterns of apical or basal dendrites

At P12 we found no effect of sex and LPS treatment on the length ($F_{(1,28)}$= 0.514, p=0.479; $F_{(1,28)}$= 0.275 p=0.604, Fig 5A) and number of the apical dendrites branches ($F_{(1,28)}$= 0.127, p=0.724; $F_{(1,28)}$= 0.254, p=0.618, Fig 5B). Neither did sholl analysis reveal any effects on the branching patterns of apical dendrites (p>0.05, Fig 5C). Similarly, no significant differences in the length, number and complexity of basal dendrites were observed between LPS and saline injected mice (p>0.05, Fig 5D-F).

At P45 we found no effect of sex and LPS treatment on the length and number of branches on apical dendrites (Fig 6A, B) or basal dendrites (Fig 6D, E). Moreover, sholl analysis revealed that the branching patterns of apical dendrite (p>0.05, Fig 6C) or basal dendrites (p>0.05, Fig 6F) were not different between the groups.

PIA increases convex hull volume of apical dendrites in males

To determine the size of the dendritic field we measured the convex hull volume of apical and basal dendrites. There was a significant sex × LPS interaction effect on convex hull volume of apical dendrites ($F_{(1,20)}$= 15.468, p=0.001) with the significant main effects of sex and LPS ($F_{(1,20)}$= 14.689, p=0.001; $F_{(1,20)}$= 4.506, p=0.046) and the partial Eta squares η2 of 0.42 and 0.18 respectively. Tukey post-hoc analysis demonstrated a significant increase of LPS treatment on convex hull volume of apical dendrites in male mice (p=0.002) with no LPS treatment effect in females (p=0.586, Fig 7A). Example of 3D reconstructed apical dendrite

convex hull from CA1 subregion of the hippocampus are shown in male saline (Fig 7B) and male LPS (Fig 7C) mice. At the level of basal dendrites, no significant difference in the convex hull volume of dendrites was observed between LPS and saline injected mice at PND45 (p>0.05, data not shown).

PIA alters neuronal spine density in a sex-dependent manner

At P12, we found significant main effect of LPS treatment ($F_{(1,28)}$= 19.840, p=0.000) on the spine number on apical dendrites, with the partial Eta square η^2 of 0.41. Games-Howell post-hoc analysis indicated a significant effect of LPS in male mice (p=0.029) with no significant LPS treatment effect in females (p=0.057, Fig 8C). There was a significant main effect of LPS treatment ($F_{(1,28)}$= 11.573, p=0.002) on the spine number on basal dendrites with the partial Eta square η2 of 0.29. Tukey post-hoc analysis indicated a significant increase of the number of spines on basal dendrites in female mice (p=0.004) with no significant LPS treatment effect in males (p=0.718, Fig 8D). At P45, we found a significant sex × LPS treatment effect on the spine number on apical dendrites ($F_{(1,20)}$= 17.803, p=0.000) and Tukey post-hoc analysis indicated a significant effect of LPS treatment in male mice (p=0.003) with no LPS treatment effect in females (p=0.244, Fig 8E). On basal dendrites, there were no effect of sex or LPS treatment on the spine number and spine density (p>0.05, Fig 8F).

PIA remodels spine morphology in a sex-dependent manner

Spine morphology is a crucial determinant of structural stability and function, so we next investigated effects of PIA on spine morphology. At P12 we found significant main effect of LPS treatment on spine area, spine length, spine diameter and spine neck length ($F_{(1,28)}$= 18.896, p=0.000; $F_{(1,28)}$= 18.760, p=0.000; $F_{(1,28)}$= 20.127, p=0.000; $F_{(1,28)}$= 19.752, p=0.000) with the partial Eta squares η^2 of 0.40, 0.41, 0.41 and 0.43 respectively. Games-Howell post-hoc analysis showed a significant increase after LPS on the spine area (Fig 9A), spine length (Fig 9B), spine diameter (Fig 9C) and spine neck length (Fig 9D) in male mice (p=0.034, p=0.044, p=0.023, p=0.010), without effect in female mice (p=0.060, p=0.052, p=0.062, p=0.124, p=0.085). At P45, there was a significant main effect of sex and sex × LPS treatment interaction on the spine area ($F_{(1,20)}$= 6.935, p=0.016; $F_{(1,20)}$= 11.987, p=0.002) with the partial Eta squares η2 of 0.25, spine length ($F_{(1,20)}$= 5.274, p=0.033; $F_{(1,20)}$= 18.166, p=0.000) with the partial Eta squares η2 of 0.20, spine diameter ($F_{(1,20)}$= 5.283, p=0.032; $F_{(1,20)}$= 15.764, p=0.001) with the partial Eta squares η2 of 0.20 and sex × LPS treatment interaction effect on the spine neck length ($F_{(1,20)}$= 14.847, p=0.001). Tukey post-hoc analysis demonstrated a significant effect of LPS treatment on spine area (Fig 9E), spine length (Fig 9F), spine diameter (Fig 9G) and spine neck length (Fig 9H) in male mice (p=0.007, p=0.001, p=0.005, p=0.004) without effects in female mice (p=0.632, p=0.392, p=0.338, p=0.462).

PIA alters density of different types of spines in a sex-dependent manner

To examine the effect of PIA on density of functionally different classes of spines, we analyzed mushroom (mature), stubby (immature), and long-thin (immature) spines separately (Fig 10A). On apical dendrites at P12, two-way ANOVA showed no significant effect of sex and LPS treatment on the density of stubby spines ($F_{(1,28)}$= 1.148, p=0.293; $F_{(1,28)}$= 1.437, p=0.241, Fig 10B), while there were significant effects of LPS on the density of mushroom spines ($F_{(1,28)}$= 12.788, p=0.001), with the partial Eta square η^2 of 0.31, and on the density of long-thin spines ($F_{(1,28)}$= 25.119, p=0.000), with the partial Eta square η^2 of 0.47. The density of long-thin spines was increased in LPS male and female compared to respective saline group (p=0.005, p=0.011, Fig 10C) respectively, while density of mushroom spine was significantly increased only in male mice after LPS (p=0.017, Fig 8D). There were no effects of LPS on the density of different types of spines on basal dendrites (data not shown).

On apical dendrites at P45, two-way ANOVA showed no significant effect of sex and LPS treatment on densities of stubby and mushroom spines ($F_{(1,20)}$= 1.857, p=0.188; $F_{(1,20)}$= 0.163, p=0.691; $F_{(1,20)}$= 3.570, p=0.073; $F_{(1,20)}$= 0.832, p=0.373), but a significant effect of sex with sex × LPS treatment interaction on the density of long-thin spines ($F_{(1,20)}$= 4.397, p=0.049; $F_{(1,20)}$= 8.621, p=0.008, Fig 10 E-G) with the partial Eta square η^2 of 0.18. The density of long-thin spines was increased in males after LPS injection (p=0.014, Fig 10F).

PIA remodels morphology of different types of spines in a sex-dependent manner

At P12, there was no effect of LPS treatment and sex on the area ($F_{(1,28)}$= 2.71, p=0.111; $F_{(1,28)}$= 2.688, p=0.112) or the neck length of stubby spines on apical dendrites ($F_{(1,28)}$= 2.233, p=0.146; $F_{(1,28)}$= 0.895, p=0.352, data not shown). For long-thin and mushroom spines, a significant effect of LPS treatment on spine area was observed ($F_{(1,28)}$= 20.099, p=0.000; $F_{(1,28)}$= 21.191, p=0.000) with the partial Eta squares η^2 of 0.50, 0.43. The long-thin spine area was significantly larger in male LPS versus male saline (p=0.000, Fig 11A) without a difference in female mice (p=0.102, Fig 11A). Mushroom spine area was significantly larger in both male and female mice after LPS (p=0.009, p=0.023) respectively (Fig 11B). Further, there was a significant effect of LPS treatment and LPS × sex interaction on spine neck length of long-thin spines ($F_{(1,28)}$= 33.537, p=0.000; $F_{(1,28)}$= 4.801, p=0.037) with the partial Eta squares η^2 of 0.54 and of mushroom spines ($F_{(1,28)}$= 21.01, p=0.000) with the partial Eta squares η^2 of 0.42. Tukey post-hoc analysis showed significant difference in the long-thin spine neck length in male LPS versus male saline (p=0.000, Fig 11C). Games-Howell post-doc test showed significantly larger mushroom neck length in male LPS compared to the male saline group (p=0.017, Fig 11D), without changes in female mice after LPS injection (p=0.066).

At P45, there was no effect of LPS treatment and sex on the spine area and neck length of stubby spines (p>0.05, data not shown). The spine area was not affected on mushroom spines ($F_{(1,20)}$= 0.829, p=0.373; $F_{(1,20)}$= 4.232 p=0.053, Fig 11F), while there was a significant effect of sex on spine area of long-thin spines ($F_{(1,20)}$= 7.374, p=0.013) with the partial Eta squares η^2 of 0.26, as well as sex × LPS treatment interaction ($F_{(1,20)}$= 13.339, p=0.002). Spine area on long-thin spines was significantly larger in male LPS versus male saline mice (p=0.004, Fig 11E) without difference in female mice after LPS injection (p=0.630). There was a significant LPS × sex interaction on spine neck length of long-thin spines ($F_{(1,20)}$= 13.571, p=0.001). On mushroom spines, there was a significant effect of sex on spine neck length ($F_{(1,20)}$= 5.275, p=0.033) with the partial Eta squares η^2 of 0.20 and sex × LPS treatment interaction ($F_{(1,20)}$= 19.328, p=0.0000). Tukey post-hoc analysis showed significant difference in the long-thin spine neck length in male LPS versus male saline (p=0.005, Fig 11G). Also, mushroom spines had a significantly larger spine neck length in male LPS compared to male saline mice (p=0.002, Fig 11H) without changes in the female mice after LPS injection (p=0.202).

PIA alters morphology and number of Reelin+ cells in the CA1 area of the hippocampus in a sex-dependent manner

Reelin plays a vital role in synaptic plasticity during development and has been studied as a potential biomarker for autism (50) and as such we examined morphological and numerical alteration of Reelin+ cells following PIA (Fig 12D). At P12, our results showed a significant LPS × sex interaction ($F_{(1,27)}$= 5.305, p=0.029) with the significant main effect of LPS ($F_{(1,27)}$= 6.501, p=0.017) on the number of Reelin+ cells with the partial Eta square η2 of 0.19. Tukey post-hoc analysis demonstrated a selective decrease in the number of Reelin+ cells in male LPS group compared to male saline mice (p=0.001, Fig 12A) without significant numerical change in female mice (p=1.000). At the baseline level, there was a significant higher number of Reelin+ cells in male saline group versus female saline group (p=0.017, Fig 12A).

Two-way ANOVA analysis showed significant LPS × sex interaction ($F_{(1,29)}$= 4.215, p=0.05) on the volume of Reelin+ cells with the main effect of treatment ($F_{(1,29)}$= 4.932, p=0.035). Partial Eta square η^2 for the effect of treatment was 0.15 which indicated a large effect of LPS treatment on the volume of Reelin+ cells. Tukey post-hoc analysis revealed at the baseline there was no difference in the volume of the Reelin+ cells in the CA1 area between male and female saline mice (p=0.987), however the volume of Reelin+ cells in male LPS was significantly larger than male saline mice (p=0.027), while no difference was observed in female mice after perinatal LPS injection (Fig 12C).

At P45, we found a significant LPS × sex interaction ($F_{(1,27)}$= 7.042, p=0.013) with the significant main effect of LPS ($F_{(1,27)}$= 5.104, p=0.032) on the number of Reelin+ cells with the partial Eta square η^2 of 0.20. Tukey post-hoc analysis identified a selective decrease in male

LPS group compared to the male saline mice (p=0.009) without significant numerical change in the female mice (p=0.992) (Fig 12B). Two-way ANOVA analysis showed significant main effect of LPS on the volume of Reelin+ cells at P45 ($F_{(1,31)}$= 20.360, p=0.000) with the partial Eta square η^2 of 0.42 which indicated a large effect of LPS treatment on the volume of Reelin+ cells. The volume of Reelin+ cells in male LPS group was significantly smaller than in the male saline group (p=0.003, Fig 12E), with a trend of smaller size of Reelin+ cells in the LPS injected group females compared with female saline group (p=0.096, Fig 12E).

PIA reduces hippocampal mRNA expression of trans-synaptic and cellular adhesion molecules in a sex-dependent manner

Reelin-signaling regulates pre- and postsynaptic structure/function by impinging trans-synaptic adhesion proteins. Therefore, we studied presynaptic NRXN3, postsynaptic NLGN1 and nectin-1. At P12, two-way ANOVA analysis demonstrated a significant LPS × sex interaction on hippocampal mRNA expression of NLGN1 ($F_{(1,36)}$= 8.214, p=0.007) with a significant main effect of LPS treatment ($F_{(1,36)}$= 14.096, p=0.001) and the partial Eta square η^2 of 0.28. Tukey post-hoc analysis showed that the mRNA expression of NLGN1 was significantly higher in female LPS compared with female saline mice (p=0.000, Fig 13A), with no significant difference in male mice (p=0.922). Two-way ANOVA of expression of mRNA level of NRXN3 demonstrated significant LPS × sex interaction ($F_{(1,36)}$= 12.123, p=0.001), with the significant main effect of LPS treatment ($F_{(1,36)}$= 11.649, p=0.002) and with the partial Eta square η^2 of 0.24. Tukey post-hoc analysis showed that mRNA level of NRXN3 was significantly higher in female LPS compared with female saline mice (p=0.000, Fig 13B), with no significant difference in male mice (p=1.000). Two-way ANOVA of hippocampal mRNA level of nectin-1 showed significant LPS × sex interaction ($F_{(1,36)}$= 6.574, p=0.015) with the significant main effect of LPS treatment ($F_{(1,36)}$= 9.946, p=0.003) and with the partial Eta square η^2 of 0.21. Games-Howell post-hoc analysis demonstrated that the mRNA expression of nectin-1 was significantly higher in female LPS compared with female saline mice (p=0.002, Fig 13C), with no significant difference in male mice (p=0.982).

At P45, there was a significant LPS × sex interaction ($F_{(1,36)}$= 7.027, p=0.012) with the significant main effect of LPS treatment ($F_{(1,36)}$= 11.850, p=0.001) and with the partial Eta square η^2 of 0.24 on the mRNA expression of NLGN1. Games-Howell post-hoc analysis showed that the mRNA expression of NLGN1 was significantly lower in male LPS compared to the male saline mice (p=0.007, Fig 13D), with no significant difference in female mice (p=0.934). Analysis of NRXN3 mRNA expression showed significant main effect of LPS treatment ($F_{(1,36)}$= 13.094, p=0.001) with the partial Eta square η^2 of 0.26. Tukey post-hoc analysis demonstrated that NRXN3 mRNA expression was decreased in LPS males (p=0.002,

Fig 13E), but not in females (p=0.646). Two-way ANOVA analysis of nectin-1 mRNA expression showed a significant LPS x sex interaction ($F_{(1,36)}$= 5.171, p=0.029) with the significant main effect of LPS treatment ($F_{(1,36)}$= 14.198, p=0.001) and the partial Eta square η^2 of 0.28. Games-Howell post-hoc analysis showed decreased mRNA expression of nectin-1 in LPS male mice (p=0.007, Fig 13F) with no significant treatment effect in females (p=0.704).

Discussion

We show that PIA at a critical brain developmental stage in mice equivalent to preterm human infants, reduces sociability and increases repetitive behaviors in P45 adolescent male animals. As shown by diffusion kurtosis MRI, a reflective marker of tissue heterogeneity, behavioral changes were associated with sex-dependent alterations in the male brain, including brain overgrowth and abnormal microstructure in the hippocampus. Detailed 3D cell reconstruction approaches revealed morphological changes of hippocampal microglia consistent with activation, immaturity of neuronal spine development, and reduced number and size of Reelin+ cells. Expression of trans-synaptic and cell adhesion genes, known to be altered in ASD individuals, was reduced in males in the long-term after PIA. Thus, the results highlight distinct sex-dependent effects of PIA on Reelin+ cells, excitatory synapses and alterations in brain growth relevant for ASD.

Repetitive behavior and impairment in sociability are core symptoms of autism. A recent clinical study showed that inflammation in preterm children without severe neonatal brain lesions was associated with inferior social ability (51). Inflammation, through TLR activation, have been suggested to significantly contribute to ASD (52, 53). Studies indicate that the timing of immune activation during pregnancy and the neonatal period, together with other factors such as genetics, sex and type of infection, influences the vulnerability to neurodevelopmental disorders (54). Specifically, males born preterm are at increased risk for ASD (55). We found that PIA increased repetitive behavior in both male and female mice, but behavioral effects were more robust in males and only male mice showed reduced sociability. In support, studies have shown that prenatal LPS exposure during the last two-thirds of gestation result in impairment in social interactions and exploration, more in adult male than in female rats (56-58). Taken together, studies demonstrate that inflammation both before and after birth is an important etiological factor for inferior social ability.

We found larger brain volume in LPS injected males by adolescent age indicating long-term sex dependent effects on cerebral overgrowth. Clinical findings have identified brain overgrowth as an early predictor for ASD diagnosis (59, 60) and in line with our findings, it was recently shown that brain enlargement in childhood does not normalize but remains through young adulthood (61). Both increased cortical surface area (62) and cortical thickness (63) have been suggested to contribute to the overall brain size enlargement in autistic patients. Further, persistent enlargement of hippocampus has been reported (64) and structural abnormalities in the CA1 area of the hippocampus were recently highlighted in children with ASD (16). In line with these findings, we show that the volume of hippocampus

is enlarged in males after LPS and by exploring subregions of the hippocampus, we locate the changes specifically to the CA1.SR region.

The increased size of CA1.SR may be due to increased neuropil, number of cells, arborization, or misplaced cells (heterotopia) (65, 66). DKI is a valuable technique for evaluating microstructural changes in the white and grey matter e.g. during brain maturation (67) but also in neurological disorders (68). While detailed cytoarchitectural neuroimaging data is sparse in individuals with autism, diffusion tensor imaging has been used to show that mean diffusivity probability distributions of both grey and white matter shift towards a higher value in adolescent autistic individuals (69). Similarly, we demonstrate by quantitative DKI analysis a significant change to higher values of mean diffusivity distributions in the hippocampus of adolescent male mice following neonatal LPS. These changes were not followed by significant changes in mean kurtosis. We propose that these results are indicative of a situation where the extracellular space is increased, which results in increased free diffusion, but without loss of tissue compartmentalization (for which mean kurtosis can be seen as a marker). Alterations in mean diffusivity without changes in mean kurtosis have previously been interpreted to indicate increased extracellular space due to dendritic spanning volumes, rather than loss of neuronal cell bodies, synapses, or dendrites. Thus, diffusion tensor image changes observed in male LPS animals in the current study may be related to the total volume occupied by neurons as we found larger convex hull of apical dendrites in male LPS group compared with the saline group.

Given the crucial role of the CA1.SR subregion in synaptic plasticity and regulation of the excitation-inhibition balance, alterations in this brain region have been associated with hyperexcitability that may underlie pathology in autism (70). While we found that PIA did not change apical and basal dendritic complexity, there were significant age and sex-dependent effects on spine remodeling on apical dendrites in the CA1 subregion of the hippocampus. Most synapses on apical dendritic spines are excitatory and there is a strong correlation between higher levels of AMPA receptors and larger spines (bigger size of the head) (71). Thus, our findings of a consistent increase in spine density and size of spines on apical dendrites on pyramidal neurons in the male LPS group, suggest changes in expression level of AMPA resulting in excessive excitatory synapse function. Interestingly, spine density on basal dendrites, which have major inhibitory processes, transiently increased only in female neonatal LPS mice, implying that PIA resulted in time- and sex-dependent effects on the balance between excitation and inhibition at the synapse level.

During brain development, transition from immature synapses associated with long thin, dendritic spines to larger synapses associated with mushroom-shaped dendritic spines occur. An essential aspect of our study design is that we classified spines based on their shape and found that while density of both immature thin and mature mushroom spines was increased on apical dendrites in pediatric male LPS mice, only the increase in thin spines remained until adolescent age. Similarly, age-dependent transient increase in perforated hippocampal synapses, mainly comprised of mushroom spines, has been observed in Shank3 mutant mice (27). Spine geometry is of importance as it reflects spine function and correlates with release probability of vesicles in the synapse (72). Thin spines carry small or immature synapses and have a greater potential for strengthening the synapse and therefore also increased capacity for plasticity in the local network (73). Increasing evidence suggests that spine structural remodeling supports long-term potentiation (LTP) (74), and LTP induction promotes spine head enlargement, formation, and stabilization of new spines (75). Thus, our finding of an increased density and size (area and diameter of the head) of thin spines in adolescent PIA male mice suggest lack of synapse maturation with enhanced LTP.

We demonstrate increased neck-length of both thin and mushroom spines on apical dendrites in P45 PIA males. The length of the spine neck influences Ca^{2+} leak and therefore affects the dynamics of postsynaptic Ca^{2+} levels (76). The correlation between spine neck length and synaptic efficacy is inverse, therefore longer spine neck results in negligible somatic voltage contributions while shortening of spine neck leads to increases in synaptic efficacy (77). The current data support this finding, as only male LPS mice exhibited longer spine necks on apical dendrites without differences in female mice. Taken together, our results suggest a static increase in spinogenesis, mainly of immature spines, in LPS treated males, which indicates abnormal synaptic efficacy and alterations in neuronal function that might be reflected in the autistic behavioral changes in male mice following PIA.

Synapse maturation is dependent on spine pruning and microglia are believed to be essential for the pruning of spines in adolescence (78). However, our results suggest that increased spine density specifically in male LPS injected mice was unlikely due to microglia activation since we observed activated microglia in both male and female LPS mice. A previous study reported greater spine density on apical dendrites of pyramidal neurons in the cortex in ASD due to lesser synapse pruning by impaired autophagy (79, 80) suggesting that other mechanisms than microglia pruning may be involved.

To determine the possible underlying cellular mechanism of the changes in synapse development, we investigated Reelin+ cells, which are essential for forming layer-specific

hippocampal connections during development (30) and have been implicated in ASD (27). We found that male LPS mice have fewer Reelin+ cells in the hippocampus at P12 and P45 and smaller soma at P45 than saline-injected animals. Reelin is essential for early axonal branching and collateral extension in the hippocampus and deficiency in Reelin+ cells result in short axonal branches (81). A previous study showed lower reelin expression in some regions of brains from subjects with ASD (31). A recent study using data from 4 European cohorts indicated an association between autism and rs362780 RELN polymorphism (82). Perikaryal abnormalities of neurons, including smaller volumes of neurons, have been reported in 4 - to 8-year-old autistic children, which was suggested as an indicator of abnormal trajectory of neuronal growth (32). Thus, our findings show defects in Reelin+ cell development and maturation in the male LPS group similar to those observed in ASD (83).

Reelin mediates interaction between two of the most prominent trans-synaptic genes (NLGN and NRXN) (84). Trans-synaptic adhesion proteins are essential for remodeling established neuronal circuits and spine morphology during brain development (85, 86). To address the impact of PIA on molecular pathways important for synapse function, we examined the gene expression of NLGN1, NRXN-3, and nectin-1, which have been implicated in the differentiation and maturation of both excitatory and inhibitory synapses (87, 88) and important for ASD (89). While there was a transient early increase in females, LPS-treated males demonstrated a long-term decrease in expression of all three genes. These findings agree with previous studies that found decreased expression of NRXN3 mRNA in male fragile X knockout (FMR1-KO) mice while expression was increased in females (90). NLGNs have a critical role in the inhibitory and excitatory transmission balance by changing the strength of synapses rather than the number of synapses. The peak level of NLGN1 is shown at P5–8 (91), and mice with NLGN1 deletion exhibited repetitive, stereotyped grooming behaviors (92). Nectin-1 is expressed on CR cells during development (93-95), and reelin has been shown to promote the assembly of Nectin-1 adhesion sites (95). In adult animals, chronic stress resulted in the reduction of nectin-1 mRNA levels with the consequence of dendritic spine remodeling in the perirhinal cortex (96). Collectively, our results highlight trans-synaptic adhesion proteins as one of the molecular targets of sex-dependent effects by PIA.

The current study provides novel sex-dependent insights into synapse remodeling in the hippocampus in an animal model of postnatal inflammation with autism phenotype. Collectively, our results highlight the decrease in adhesion-transsynaptic genes, which may be a consequence of deficits in Reelin+ cell development. We propose that the sex-dependent deficiency in Reelin+ cells and abnormal regulation of NLGN-1, NRXN3, and nectin-1 contribute to an impaired excitatory/inhibitory balance at the synapse, thereby increasing the

risk for autistic-like behavior in males. These findings give important new cellular and molecular information on possible underlying mechanisms of the interaction of infection in preterm male infants and brain development that may underly autistic-like behavior.

Disclosures:

The authors have nothing to disclose.

Figure Legends

Figure 1. Effects of postnatal immune activation (PIA) on brain, hippocampi and hippocampal subregions volume at P45.

Volume measurements of the whole brain (excluding olfactory bulb and cerebellum) (A, C) and entire hippocampi (B, D) were performed on MRI images at P45. Volume measurement of hippocampal granular cell layer (GCL) (E) and CA1 stratum radiatum (CA1.SR) (F) subregions were performed on Nissl-stained sections at P45. PIA resulted in increased volume of the whole brain and hippocampus and CA1.SR region in male mice. Ex-vivo images were generated using ITK-snap and ParaView-5.8.0-RC1-Windows-Python3.7 software (Ayachit, Utkarsh, *The ParaView Guide: A Parallel Visualization Application*, Kitware, 2015, ISBN 978-1930934306). *p<0.05, **p<0.01, *** p<0.001.

Figure 2. Effects of postnatal immune activation (PIA) on MRI kurtosis at P45.

Mean diffusivity (MD) and mean kurtosis (MK) measurements were acquired from MRI images at P45 in male and female mice following PIA. Example showing MD images in groups at the hippocampal level (A). Histograms showing that the distribution of MD in dorsal and ventral hippocampus in PIA males (brown) was increased compared to saline males (blue) (B), while MD was decreased in PIA females (brown) compared to saline females (blue) (C). There were no changes in mean kurtosis (MK) in dorsal or ventral hippocampus in males (D) and females (E) in saline (blue) and LPS (brown) treated animals. MD reflects overall water mobility (averaged over all directions) and is given in units of um^2/ms." In the histogram figure, ** indicates significantly different distributions at the p<0.01 level using Matlab's Two-sample Kolmogorov-Smirnov goodness-of-fit hypothesis test. This tests if independent random samples, X1 and X2, are drawn from the same underlying continuous population.

Figure 3. Effects of postnatal immune activation (PIA) on microglia morphology at P12 and P45.

Microglia were identified by Iba-1 immunohistochemistry in the hippocampus at P12 (A, B, C) and P45 (E, F, G). Microglia morphology analysis indicated less ramification by having shorter process lengths and smaller numbers of processes in CA1.SR subregion of the hippocampus in male and female PIA animals compared to saline groups at P12 (A, B) and P45 (E, F); Branching pattern analysis of microglia demonstrated that the number of branching intersections at various distances away from the cell soma was significantly lower in LPS group versus saline group at P12 (C) and P45 (G), independent of sex. Examples of 3-D reconstructed microglia in the CA1.SR subregion of hippocampus in male saline mouse (D) and male LPS mouse (H); *p<0.05, **p<0.01, ***p<0.001.

Figure 4. Effects of postnatal immune activation (PIA) on autistic-like behaviors at P45. Stereotypic and repetitive behavior was investigated by the marble burying test (A) and sociability by the three-chamber test (B, C) at P45. Marble burying test showed a significantly higher number of buried marbles in male and female LPS mice compared to saline groups (A). There were significant main effects of LPS treatment on sociability (B) and social index (C) in male mice only. *p<0.05, **p<0.01, ***p<0.001.

Figure 5. Effects of postnatal immune activation (PIA) on the apical and basal dendritic arborizations and complexity in the CA1 subregion of hippocampus in mice at P12. Analysis of apical and basal dendritic morphology was investigated on Golgi-Cox impregnated pyramidal neurons in the CA1 subregion of hippocampus in mice at P12. Apical (A, B) and basal (D, E) dendritic lengths and numbers did not change one week after LPS injection in males or females. No differences were observed in the complexity of apical (C) and basal (F) dendrites one week after LPS injection in males or females.

Figure 6. Effects of postnatal immune activation (PIA) on apical and basal dendritic arborization and complexity in the CA1 subregion of hippocampus in at P45. Analysis of apical and basal dendritic morphology was investigated on Golgi-Cox impregnated pyramidal neurons in the CA1 subregion of hippocampus in mice at P45. Apical (A-C) and basal (D-F) dendritic lengths and numbers and complexity did not change 40 days after LPS injection in either males or females.

Figure 7. Effect of postnatal immune activation (PIA) on convex hull volume on apical and dendrites at P45 Convex hull volume on apical dendrites was investigated on Golgi-Cox impregnated pyramidal neurons in the CA1 subregion of hippocampus in mice at P45. PIA increased the convex hull volume of apical dendrites in male mice 40 days after LPS injection (A). ** p<0.01. Example of 3D reconstructed apical dendrite convex hull from CA1 subregion of the hippocampus in male saline (B) and male LPS (C) mice.

Figure 8. PIA alters neuronal spine density in a time- and sex-dependent manner Analysis of spines on 3D reconstructed apical (A) and basal (B) dendrites was investigated on Golgi-Cox impregnated pyramidal neurons in the CA1 subregion of hippocampus in mice at P12 (C, D) and P45 (E, F). The spine density on apical dendrites was significantly increased one week (C) and 40 days (E) after LPS injection in male mice. The spine density on basal

dendrites was significantly increased one week (D) after LPS injection in female mice without significant changes at P45 (F). *p<0.05, **p<0.01.

Figure 9. PIA remodels spine morphology in a time- and sex-dependent manner

Morphology of spines, including spine area (A, E), spine length (B, F), spine diameter (C, G) and spine neck length (D, H) was investigated on 3-D reconstructed apical dendrites on Golgi-Cox impregnated pyramidal neurons in the CA1 subregion of hippocampus in mice at P12 (A-D) and P45 (E-H). Spine area, length, diameter and neck length were enlarged in PIA males at P12 and P45. *p<0.05, **p<0.01, ***p<0.001.

Figure 10. PIA alters density of different types of spines in a time- and sex-dependent manner

Density of spine types, including long-thin (green arrow), mushroom (orange arrow) and stubby (blue arrow) (A), was investigated on 3-D reconstructed apical dendrites on Golgi-Cox impregnated pyramidal neurons in the CA1 subregion of hippocampus in mice at P12 (B, C, D) and P45 (E, F, G). The density of stubby spines was not different between groups at P12 (B) or P45 (E). Density of long-thin spines was increased in both PIA male and female mice at P12 (C), but only in PIA males at P45 (F). The density of mushroom spines was increased in PIA males only at P12 (D). *p<0.05, **p<0.01.

Figure 11. PIA remodels morphology of different types of spines in a time- and sex-dependent manner.

Morphology of long-thin (A, C, E, G) and mushroom (B, D, F, H) spines, including spine area (A, B, E, F) and spine neck length (C, D, G, H) was investigated on 3-D reconstructed apical dendrites on Golgi-Cox impregnated pyramidal neurons in the CA1 subregion of hippocampus in mice at P12 (A-D) and P45 (E-H). The spine area and neck length of long-thin spines was increased at P12 (A, C) and P45 (E, G) in male PIA mice. Spine area on mushroom spines was increased on both male and females at P12 (B), while neck length of mushroom spines was only increased in PIA males at P12 (D) and P45 (H). *p<0.05, **p<0.01, ***p<0.001.

Figure 12. Effects of postnatal immune activation (PIA) on Reelin+ cells at P12 and P45.

Reelin immunohistochemistry (D) was performed at P12 and P45 and number (A, B) and cell soma volume (C, E) of Reelin+ cells analyzed by unbiased stereological methods. There were significantly fewer Reelin+ cells in saline female compared to saline male mice at both ages. PIA males had fewer Reelin+ cells compared to saline treated males at P12 (A) and P45 (B). Reelin+ cells volume was transiently increased at P12 in PIA males (C), while decreased at P45 (E). Volume measurement were determined by applying spatial rotator estimator

independent of the orientation under a 100× objective lens. Scale bar is 35 μm (D). *p<0.05, **p<0.01, ***p<0.001.

Figure 13. Effects of postnatal immune activation (PIA) on synaptic cell adhesion mRNA expression at P12 and P45.

Levels of mRNA expression for neuroligin-1 (NLGN1), neurexin-3 (NRXN-3), and Nectin-1 were determined by RT-PCR in the hippocampus at P12 (A-C) and P45 (D-F). NLGN1, NRXN-3 and Nectin-1 mRNA expression was significantly increased in female PIA at P12 (A-C), while the mRNA expression for all three genes was decreased in male PIA at P45 (D-F). ** p<0.01, ***p<0.001.

Supplementary Fig 1: Significant effect of PIA on the morphology of spines on the basal dendrites in female mice by showing significant enlargement in spine area (A), spine length (B), spine diameter (C), spine neck length (D) and spine neck diameter (E) one week after injection (independent of the type of spines). *p<0.05.

Supplementary Fig 2: No effect of PIA on the morphology of spines on the basal dendrites, including spine area (A), spine length (B), spine diameter (C), and spine neck length (D) (independent of the type of spines) 40 days after injection.

Supplementary Fig 3: Effect of PIA on the morphology of stubby (A, D, G), long-thin (B, E, H), and mushroom (C, F, I) spines on the basal dendrites one week after LPS injection, *p<0.05, ***p<0.001.

Funding

This study was supported by Lundbeck Foundation (R322-2019-2721), Mary von Sydows Foundation (2020-3420), Magn. Bergvalls Foundation (2020-03756), HKH Kronprinsessan Lovisas Foundation, Axel Tielmans Foundation (2020-00559), Swedish Research Council (VR-2017-01409), Åhlen Foundation, Public Health Service at the Sahlgrenska University Hospital (ALFGBG-722491), Swedish Brain Foundation (FO2019-0270), National Institute of Health (R01 HL139685) and National Institute of Health (R01 NS103483).

References

1. Blencowe H, Cousens S, Chou D, Oestergaard M, Say L, Moller AB, et al. Born too soon: the global epidemiology of 15 million preterm births. Reprod Health. 2013;10 Suppl 1:S2.
2. Strunk T, Inder T, Wang X, Burgner D, Mallard C, Levy O. Infection-induced inflammation and cerebral injury in preterm infants. Lancet Infect Dis. 2014;14(8):751-62.
3. Moore T, Johnson S, Hennessy E, Marlow N. Screening for autism in extremely preterm infants: problems in interpretation. Dev Med Child Neurol. 2012;54(6):514-20.
4. Hagberg H, Gressens P, Mallard C. Inflammation during fetal and neonatal life: implications for neurologic and neuropsychiatric disease in children and adults. Ann Neurol. 2012;71(4):444-57.
5. Hagberg H, Mallard C, Ferriero DM, Vannucci SJ, Levison SW, Vexler ZS, et al. The role of inflammation in perinatal brain injury. Nat Rev Neurol. 2015;11(4):192-208.
6. Christensen DL, Maenner MJ, Bilder D, Constantino JN, Daniels J, Durkin MS, et al. Prevalence and Characteristics of Autism Spectrum Disorder Among Children Aged 4 Years - Early Autism and Developmental Disabilities Monitoring Network, Seven Sites, United States, 2010, 2012, and 2014. MMWR Surveill Summ. 2019;68(2):1-19.
7. Harrop C, Jones D, Zheng S, Nowell SW, Boyd BA, Sasson N. Sex differences in social attention in autism spectrum disorder. Autism Res. 2018;11(9):1264-75.
8. Prosperi M, Turi M, Guerrera S, Napoli E, Tancredi R, Igliozzi R, et al. Sex differences in Autism Spectrum Disorder: an investigation on core symptoms and psychiatric comorbidity in preschoolers. Frontiers in Integrative Neuroscience. 2020;14:62.
9. Little LM, Wallisch A, Salley B, Jamison R. Do early caregiver concerns differ for girls with autism spectrum disorders? Autism. 2017;21(6):728-32.
10. Hallmayer J, Cleveland S, Torres A, Phillips J, Cohen B, Torigoe T, et al. Genetic Heritability and Shared Environmental Factors Among Twin Pairs With Autism. Arch Gen Psychiat. 2011;68(11):1095-102.
11. Taylor MJ, Rosenqvist MA, Larsson H, Gillberg C, D'Onofrio BM, Lichtenstein P, et al. Etiology of Autism Spectrum Disorders and Autistic Traits Over Time. JAMA Psychiatry. 2020;77(9):936-43.
12. Vargas DL, Nascimbene C, Krishnan C, Zimmerman AW, Pardo CA. Neuroglial activation and neuroinflammation in the brain of patients with autism. Ann Neurol. 2005;57(1):67-81.
13. Enstrom AM, Onore CE, Van de Water JA, Ashwood P. Differential monocyte responses to TLR ligands in children with autism spectrum disorders. Brain Behav Immun. 2010;24(1):64-71.

14. Alexander C, Rietschel ET. Bacterial lipopolysaccharides and innate immunity. J Endotoxin Res. 2001;7(3):167-202.
15. Custodio CS, Mello BSF, Filho A, de Carvalho Lima CN, Cordeiro RC, Miyajima F, et al. Neonatal Immune Challenge with Lipopolysaccharide Triggers Long-lasting Sex- and Age-related Behavioral and Immune/Neurotrophic Alterations in Mice: Relevance to Autism Spectrum Disorders. Mol Neurobiol. 2018;55(5):3775-88.
16. Li G, Chen MH, Li G, Wu D, Lian C, Sun Q, et al. A Longitudinal MRI Study of Amygdala and Hippocampal Subfields for Infants with Risk of Autism. Graph Learn Med Imaging (2019). 2019;11849:164-71.
17. Mandai K, Rikitake Y, Mori M, Takai Y. Nectins and nectin-like molecules in development and disease. Current topics in developmental biology. 2015;112:197-231.
18. Ichtchenko K, Hata Y, Nguyen T, Ullrich B, Missler M, Moomaw C, et al. Neuroligin 1: a splice site-specific ligand for beta-neurexins. Cell. 1995;81(3):435-43.
19. Kwon HB, Kozorovitskiy Y, Oh WJ, Peixoto RT, Akhtar N, Saulnier JL, et al. Neuroligin-1-dependent competition regulates cortical synaptogenesis and synapse number. Nat Neurosci. 2012;15(12):1667-74.
20. Vaags AK, Lionel AC, Sato D, Goodenberger M, Stein QP, Curran S, et al. Rare Deletions at the Neurexin 3 Locus in Autism Spectrum Disorder. Am J Hum Genet. 2012;90(1):133-41.
21. Yuan HM, Wang QM, Liu YH, Yang W, He Y, Gusella JF, et al. A rare exonic NRXN3 deletion segregating with neurodevelopmental and neuropsychiatric conditions in a three-generation Chinese family. Am J Med Genet B. 2018;177(6):589-95.
22. Glessner JT, Wang K, Cai G, Korvatska O, Kim CE, Wood S, et al. Autism genome-wide copy number variation reveals ubiquitin and neuronal genes. Nature. 2009;459(7246):569-73.
23. Tejada MI, Elcoroaristizabal X, Ibarluzea N, Botella MP, de la Hoz AB, Ocio I. A novel nonsense homozygous variant in the NLGN1 gene found in a pair of monozygotic twin brothers with intellectual disability and autism. Clin Genet. 2019;95(2):339-40.
24. Varghese M, Keshav N, Jacot-Descombes S, Warda T, Wicinski B, Dickstein DL, et al. Autism spectrum disorder: neuropathology and animal models. Acta Neuropathol. 2017;134(4):537-66.
25. Mizoguchi A, Nakanishi H, Kimura K, Matsubara K, Ozaki-Kuroda K, Katata T, et al. Nectin: an adhesion molecule involved in formation of synapses. J Cell Biol. 2002;156(3):555-65.
26. Lim ST, Chang A, Giuliano RE, Federoff HJ. Ectodomain shedding of nectin-1 regulates the maintenance of dendritic spine density. Journal of Neurochemistry. 2012;120(5):741-51.

27. Lammert DB, Howell BW. RELN Mutations in Autism Spectrum Disorder. Front Cell Neurosci. 2016;10:84.
28. Smith PL, Hagberg H, Naylor AS, Mallard C. Neonatal peripheral immune challenge activates microglia and inhibits neurogenesis in the developing murine hippocampus. Dev Neurosci. 2014;36(2):119-31.
29. Semple BD, Blomgren K, Gimlin K, Ferriero DM, Noble-Haeusslein LJ. Brain development in rodents and humans: Identifying benchmarks of maturation and vulnerability to injury across species. Prog Neurobiol. 2013;106-107:1-16.
30. Deacon RM. Digging and marble burying in mice: simple methods for in vivo identification of biological impacts. Nat Protoc. 2006;1(1):122-4.
31. Yang M, Silverman JL, Crawley JN. Automated three-chambered social approach task for mice. Curr Protoc Neurosci. 2011;Chapter 8:Unit 8 26.
32. Haida O, Al Sagheer T, Balbous A, Francheteau M, Matas E, Soria F, et al. Sex-dependent behavioral deficits and neuropathology in a maternal immune activation model of autism. Transl Psychiatry. 2019;9(1):124.
33. Gundersen HJ. The smooth fractionator. J Microsc. 2002;207(Pt 3):191-210.
34. Treccani G, Ardalan M, Chen F, Musazzi L, Popoli M, Wegener G, et al. S-Ketamine Reverses Hippocampal Dendritic Spine Deficits in Flinders Sensitive Line Rats Within 1 h of Administration. Mol Neurobiol. 2019;56(11):7368-79.
35. Sholl DA. Dendritic organization in the neurons of the visual and motor cortices of the cat. J Anat. 1953;87(4):387-406.
36. Kim W, Im MJ, Park CH, Lee CJ, Choi S, Yoon BJ. Remodeling of the dendritic structure of the striatal medium spiny neurons accompanies behavioral recovery in a mouse model of Parkinson's disease. Neurosci Lett. 2013;557 Pt B:95-100.
37. Ardalan M, Rafati AH, Nyengaard JR, Wegener G. Rapid antidepressant effect of ketamine correlates with astroglial plasticity in the hippocampus. Br J Pharmacol. 2017;174(6):483-92.
38. Gundersen HJ. Stereology of arbitrary particles. A review of unbiased number and size estimators and the presentation of some new ones, in memory of William R. Thompson. J Microsc. 1986;143(Pt 1):3-45.
39. Ardalan M, Wegener G, Polsinelli B, Madsen TM, Nyengaard JR. Neurovascular plasticity of the hippocampus one week after a single dose of ketamine in genetic rat model of depression. Hippocampus. 2016;26(11):1414-23.
40. Pelkey KA, Chittajallu R, Craig MT, Tricoire L, Wester JC, McBain CJ. Hippocampal GABAergic Inhibitory Interneurons. Physiol Rev. 2017;97(4):1619-747.
41. Rasmusson A, Hahn U, Larsen JO, Gundersen HJG, Jensen EBV, Nyengaard JR. The spatial rotator. J Microsc. 2013;250(2):88-100.

42. Gundersen HJ, Bagger P, Bendtsen TF, Evans SM, Korbo L, Marcussen N, et al. The new stereological tools: disector, fractionator, nucleator and point sampled intercepts and their use in pathological research and diagnosis. APMIS. 1988;96(10):857-81.
43. Qvist P, Eskildsen SF, Hansen B, Baragji M, Ringgaard S, Roovers J, et al. Brain volumetric alterations accompanied with loss of striatal medium-sized spiny neurons and cortical parvalbumin expressing interneurons in Brd1(+/-) mice. Sci Rep. 2018;8(1):16486.
44. Hansen B, Lund TE, Sangill R, Jespersen SN. Experimentally and computationally fast method for estimation of a mean kurtosis. Magn Reson Med. 2013;69(6):1754-60.
45. Hansen B, Khan AR, Shemesh N, Lund TE, Sangill R, Eskildsen SF, et al. White matter biomarkers from fast protocols using axially symmetric diffusion kurtosis imaging. NMR Biomed. 2017;30(9).
46. Jensen JH, Helpern JA, Ramani A, Lu H, Kaczynski K. Diffusional kurtosis imaging: the quantification of non-gaussian water diffusion by means of magnetic resonance imaging. Magn Reson Med. 2005;53(6):1432-40.
47. Yushkevich PA, Piven J, Hazlett HC, Smith RG, Ho S, Gee JC, et al. User-guided 3D active contour segmentation of anatomical structures: significantly improved efficiency and reliability. Neuroimage. 2006;31(3):1116-28.
48. Sparks BF, Friedman SD, Shaw DW, Aylward EH, Echelard D, Artru AA, et al. Brain structural abnormalities in young children with autism spectrum disorder. Neurology. 2002;59(2):184-92.
49. Hansen B. Diffusion Kurtosis Imaging as a Tool in Neurotoxicology. Neurotox Res. 2020;37(1):41-7.
50. Folsom TD, Fatemi SH. The involvement of Reelin in neurodevelopmental disorders. Neuropharmacology. 2013;68:122-35.
51. Giraud A, Chaux R, Allard M-J, Celle M, Teyssier G, Roche F, et al. Perinatal inflammation is associated with social and motor impairments in preterm children without severe neonatal brain injury. European Journal of Paediatric Neurology. 2020;28:126-32.
52. Ashwood P, Krakowiak P, Hertz-Picciotto I, Hansen R, Pessah I, Van de Water J. Elevated plasma cytokines in autism spectrum disorders provide evidence of immune dysfunction and are associated with impaired behavioral outcome. Brain Behav Immun. 2011;25(1):40-5.
53. Enstrom A, Onore C, Hertz-Picciotto I, Hansen R, Croen L, Van de Water J, et al. Detection of IL-17 and IL-23 in Plasma Samples of Children with Autism. Am J Biochem Biotechnol. 2008;4(2):114-20.
54. Ardalan M, Chumak T, Vexler Z, Mallard C. Sex-Dependent Effects of Perinatal Inflammation on the Brain: Implication for Neuro-Psychiatric Disorders. Int J Mol Sci. 2019;20(9).

55. Cogley C, O'Reilly H, Bramham J, Downes M. A Systematic Review of the Risk Factors for Autism Spectrum Disorder in Children Born Preterm. Child Psychiat Hum D. 2020.
56. Basta-Kaim A, Fijal K, Slusarczyk J, Trojan E, Glombik K, Budziszewska B, et al. Prenatal administration of lipopolysaccharide induces sex-dependent changes in glutamic acid decarboxylase and parvalbumin in the adult rat brain. Neuroscience. 2015;287:78-92.
57. Taylor PV, Veenema AH, Paul MJ, Bredewold R, Isaacs S, de Vries GJ. Sexually dimorphic effects of a prenatal immune challenge on social play and vasopressin expression in juvenile rats. Biol Sex Differ. 2012;3(1):15.
58. Carlezon WA, Kim W, Missig G, Finger BC, Landino SM, Alexander AJ, et al. Maternal and early postnatal immune activation produce sex-specific effects on autism-like behaviors and neuroimmune function in mice. Sci Rep-Uk. 2019;9.
59. Hazlett HC, Gu H, Munsell BC, Kim SH, Styner M, Wolff JJ, et al. Early brain development in infants at high risk for autism spectrum disorder. Nature. 2017;542(7641):348-51.
60. Shen MD, Nordahl CW, Young GS, Wootton-Gorges SL, Lee A, Liston SE, et al. Early brain enlargement and elevated extra-axial fluid in infants who develop autism spectrum disorder. Brain. 2013;136(Pt 9):2825-35.
61. Yankowitz LD, Herrington JD, Yerys BE, Pereira JA, Pandey J, Schultz RT. Evidence against the "normalization" prediction of the early brain overgrowth hypothesis of autism. Mol Autism. 2020;11(1):51.
62. Ohta H, Nordahl CW, Iosif AM, Lee A, Rogers S, Amaral DG. Increased Surface Area, but not Cortical Thickness, in a Subset of Young Boys With Autism Spectrum Disorder. Autism Res. 2016;9(2):232-48.
63. Khundrakpam BS, Lewis JD, Kostopoulos P, Carbonell F, Evans AC. Cortical Thickness Abnormalities in Autism Spectrum Disorders Through Late Childhood, Adolescence, and Adulthood: A Large-Scale MRI Study. Cereb Cortex. 2017;27(3):1721-31.
64. Schumann CM, Hamstra J, Goodlin-Jones BL, Lotspeich LJ, Kwon H, Buonocore MH, et al. The amygdala is enlarged in children but not adolescents with autism; the hippocampus is enlarged at all ages. J Neurosci. 2004;24(28):6392-401.
65. Raymond GV, Bauman ML, Kemper TL. Hippocampus in autism: a Golgi analysis. Acta Neuropathol. 1996;91(1):117-9.
66. Weidenheim KM, Goodman L, Dickson DW, Gillberg C, Rastam M, Rapin I. Etiology and pathophysiology of autistic behavior: clues from two cases with an unusual variant of neuroaxonal dystrophy. J Child Neurol. 2001;16(11):809-19.
67. Lebel C, Walker L, Leemans A, Phillips L, Beaulieu C. Microstructural maturation of the human brain from childhood to adulthood. Neuroimage. 2008;40(3):1044-55.

68. Tietze A, Hansen MB, Ostergaard L, Jespersen SN, Sangill R, Lund TE, et al. Mean Diffusional Kurtosis in Patients with Glioma: Initial Results with a Fast Imaging Method in a Clinical Setting. Am J Neuroradiol. 2015;36(8):1472-8.
69. Groen WB, Buitelaar JK, van der Gaag RJ, Zwiers MP. Pervasive microstructural abnormalities in autism: a DTI study. J Psychiatry Neurosci. 2011;36(1):32-40.
70. Guang S, Pang N, Deng X, Yang L, He F, Wu L, et al. Synaptopathology Involved in Autism Spectrum Disorder. Front Cell Neurosci. 2018;12:470.
71. Kasai H, Matsuzaki M, Noguchi J, Yasumatsu N, Honkura N. [Structure-stability-function relationships of dendritic spines]. Tanpakushitsu Kakusan Koso. 2004;49(3 Suppl):276-81.
72. Nimchinsky EA, Sabatini BL, Svoboda K. Structure and function of dendritic spines. Annu Rev Physiol. 2002;64:313-53.
73. Berry KP, Nedivi E. Spine Dynamics: Are They All the Same? Neuron. 2017;96(1):43-55.
74. Gipson CD, Olive MF. Structural and functional plasticity of dendritic spines - root or result of behavior? Genes Brain Behav. 2017;16(1):101-17.
75. Chidambaram SB, Rathipriya AG, Bolla SR, Bhat A, Ray B, Mahalakshmi AM, et al. Dendritic spines: Revisiting the physiological role. Prog Neuropsychopharmacol Biol Psychiatry. 2019;92:161-93.
76. Noguchi J, Matsuzaki M, Ellis-Davies GC, Kasai H. Spine-neck geometry determines NMDA receptor-dependent Ca2+ signaling in dendrites. Neuron. 2005;46(4):609-22.
77. Araya R, Vogels TP, Yuste R. Activity-dependent dendritic spine neck changes are correlated with synaptic strength. Proc Natl Acad Sci U S A. 2014;111(28):E2895-904.
78. Mallya AP, Wang HD, Lee HNR, Deutch AY. Microglial Pruning of Synapses in the Prefrontal Cortex During Adolescence. Cereb Cortex. 2019;29(4):1634-43.
79. Tang G, Gudsnuk K, Kuo SH, Cotrina ML, Rosoklija G, Sosunov A, et al. Loss of mTOR-dependent macroautophagy causes autistic-like synaptic pruning deficits. Neuron. 2014;83(5):1131-43.
80. Werling DM, Parikshak NN, Geschwind DH. Gene expression in human brain implicates sexually dimorphic pathways in autism spectrum disorders. Nat Commun. 2016;7:10717.
81. DelRio JA, Heimrich B, Borrell V, Forster E, Drakew A, Alcantara S, et al. A role for Cajal-Retzius cells and reelin in the development of hippocampal connections. Nature. 1997;385(6611):70-4.
82. Holt R, Barnby G, Maestrini E, Bacchelli E, Brocklebank D, Sousa I, et al. Linkage and candidate gene studies of autism spectrum disorders in European populations. Eur J Hum Genet. 2010;18(9):1013-9.

83. Fatemi SH. The role of Reelin in pathology of autism. Mol Psychiatry. 2002;7(9):919-20.
84. Niu S, Renfro A, Quattrocchi CC, Sheldon M, D'Arcangelo G. Reelin promotes hippocampal dendrite development through the VLDLR/ApoER2-Dab1 pathway. Neuron. 2004;41(1):71-84.
85. Holtmaat A, Svoboda K. Experience-dependent structural synaptic plasticity in the mammalian brain. Nat Rev Neurosci. 2009;10(9):647-58.
86. Alvarez VA, Sabatini BL. Anatomical and physiological plasticity of dendritic spines. Annu Rev Neurosci. 2007;30:79-97.
87. Bottos A, Destro E, Rissone A, Graziano S, Cordara G, Assenzio B, et al. The synaptic proteins neurexins and neuroligins are widely expressed in the vascular system and contribute to its functions. Proc Natl Acad Sci U S A. 2009;106(49):20782-7.
88. Krueger DD, Tuffy LP, Papadopoulos T, Brose N. The role of neurexins and neuroligins in the formation, maturation, and function of vertebrate synapses. Curr Opin Neurobiol. 2012;22(3):412-22.
89. Sudhof TC. Neuroligins and neurexins link synaptic function to cognitive disease. Nature. 2008;455(7215):903-11.
90. Lai JK, Doering LC, Foster JA. Developmental expression of the neuroligins and neurexins in fragile X mice. J Comp Neurol. 2016;524(4):807-28.
91. Song JY, Ichtchenko K, Sudhof TC, Brose N. Neuroligin 1 is a postsynaptic cell-adhesion molecule of excitatory synapses. Proc Natl Acad Sci U S A. 1999;96(3):1100-5.
92. Blundell J, Blaiss CA, Etherton MR, Espinosa F, Tabuchi K, Walz C, et al. Neuroligin-1 deletion results in impaired spatial memory and increased repetitive behavior. J Neurosci. 2010;30(6):2115-29.
93. Lim ST, Lim KC, Giuliano RE, Federoff HJ. Temporal and spatial localization of nectin-1 and l-afadin during synaptogenesis in hippocampal neurons. J Comp Neurol. 2008;507(2):1228-44.
94. Rikitake Y, Mandai K, Takai Y. The role of nectins in different types of cell-cell adhesion. J Cell Sci. 2012;125(Pt 16):3713-22.
95. Gil-Sanz C, Franco SJ, Martinez-Garay I, Espinosa A, Harkins-Perry S, Muller U. Cajal-Retzius cells instruct neuronal migration by coincidence signaling between secreted and contact-dependent guidance cues. Neuron. 2013;79(3):461-77.
96. Gong Q, Su YA, Wu C, Si TM, Deussing JM, Schmidt MV, et al. Chronic Stress Reduces Nectin-1 mRNA Levels and Disrupts Dendritic Spine Plasticity in the Adult Mouse Perirhinal Cortex. Front Cell Neurosci. 2018;12:67.

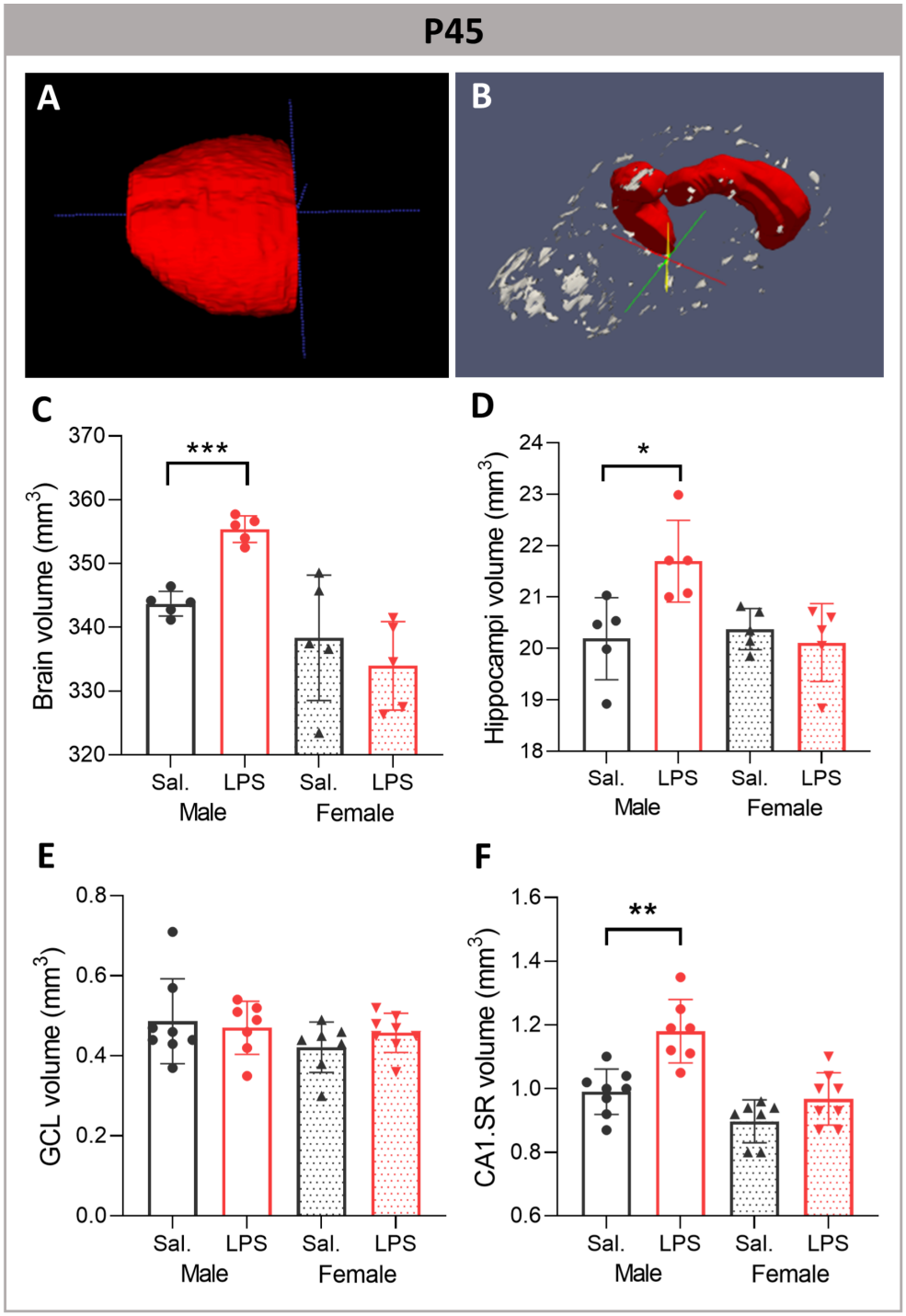
P45
A
B
C
Brain volume (mm3)
370
360
350
340
330
320
***
Sal.
LPS
Sal.
LPS
Male
Female
D
Hippocampi volume (mm3)
24
23
22
21
20
19
18
*
Sal.
LPS
Sal.
LPS
Male
Female
E
GCL volume (mm3)
0.8
0.6
0.4
0.2
0.0
Sal.
LPS
Sal.
LPS
Male
Female
F
CA1.SR volume (mm3)
1.6
1.4
1.2
1.0
0.8
0.6
**
Sal.
LPS
Sal.
LPS
Male
Female

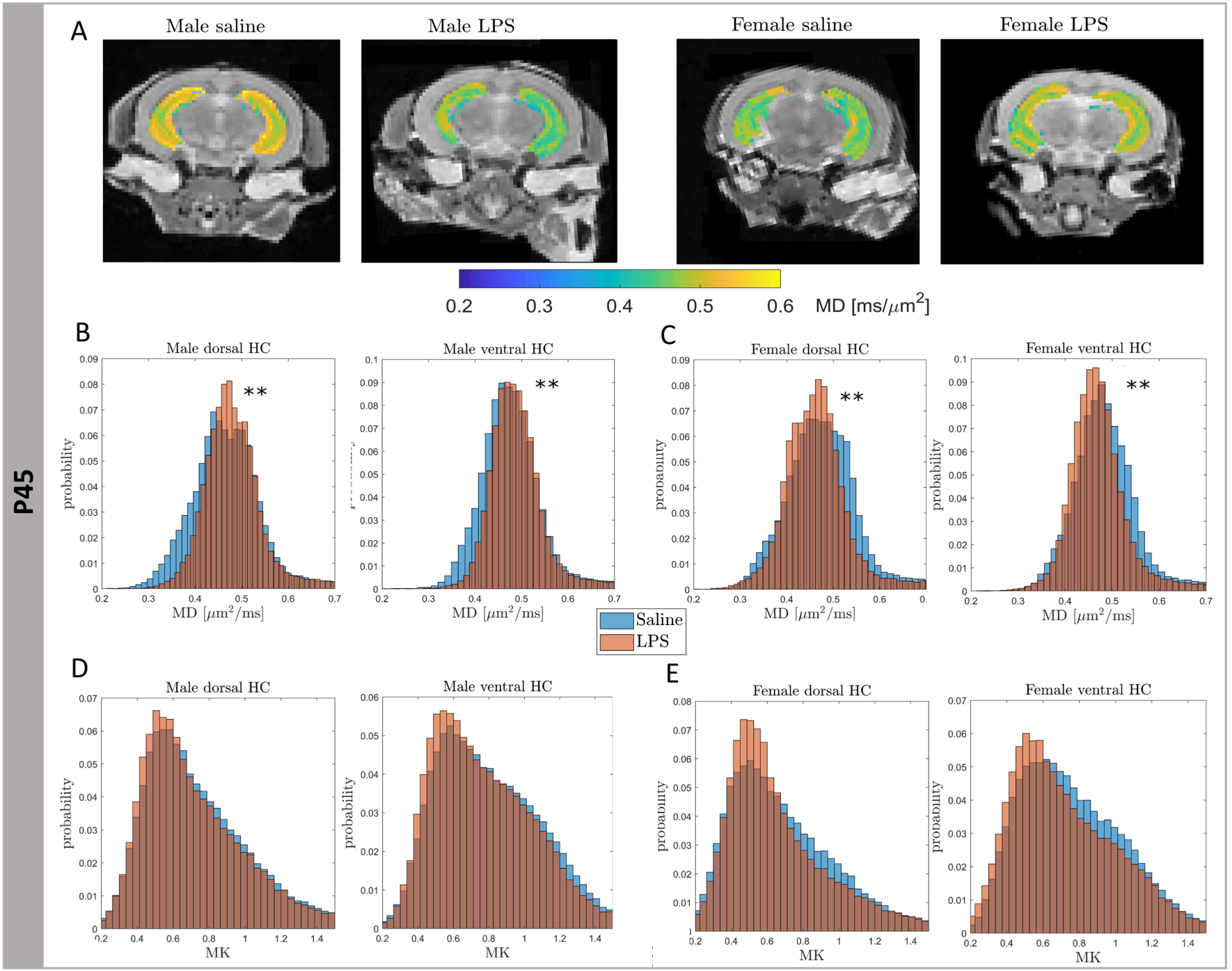
P45
A
Male saline
Male LPS
Female saline
Female LPS
0.2
0.3
0.4
0.5
0.6
MD [ms/μm²]
B
Male dorsal HC
Male ventral HC
C
Female dorsal HC
Female ventral HC
**
probability
MD [μm²/ms]
Saline
LPS
D
Male dorsal HC
Male ventral HC
E
Female dorsal HC
Female ventral HC
MK

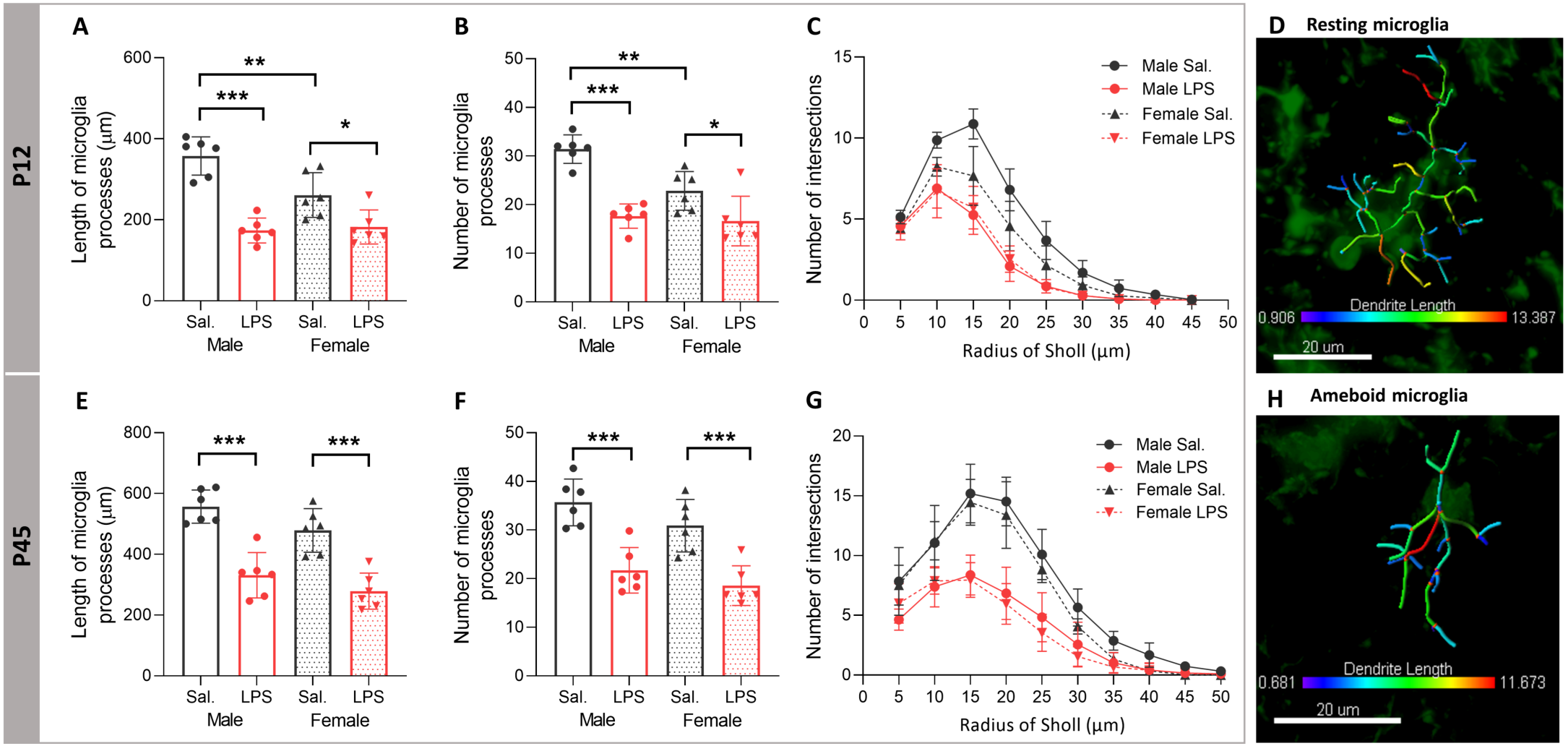
P12
P45
A
B
C
D Resting microglia
E
F
G
H Ameboid microglia
Length of microglia processes (µm)
Number of microglia processes
Number of intersections
Radius of Sholl (µm)
Sal.
LPS
Male
Female
Male Sal.
Male LPS
Female Sal.
Female LPS
Dendrite Length
0.906
13.387
0.681
11.673
20 um

P45

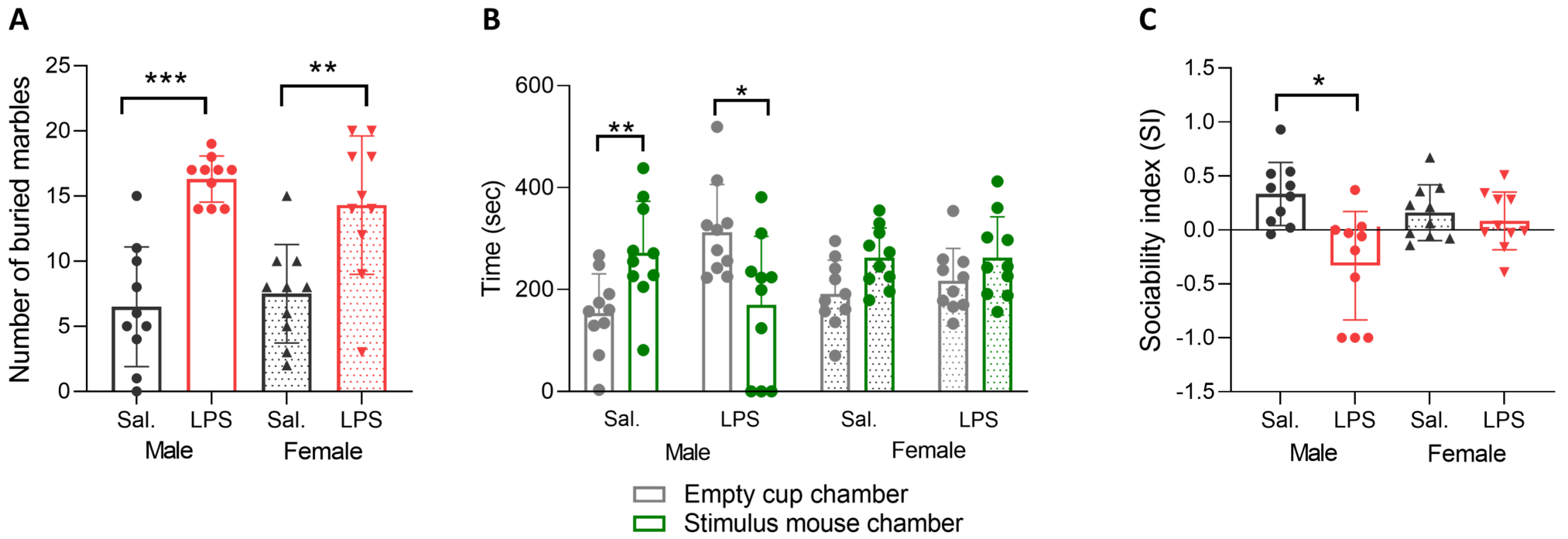
A
Number of buried marbles
25
20
15
10
5
0
***
**
Sal.
LPS
Sal.
LPS
Male
Female
B
Time (sec)
600
400
200
0
**
*
Sal.
LPS
Sal.
LPS
Male
Female
Empty cup chamber
Stimulus mouse chamber
C
Sociability index (SI)
1.5
1.0
0.5
0.0
-0.5
-1.0
-1.5
*
Sal.
LPS
Sal.
LPS
Male
Female

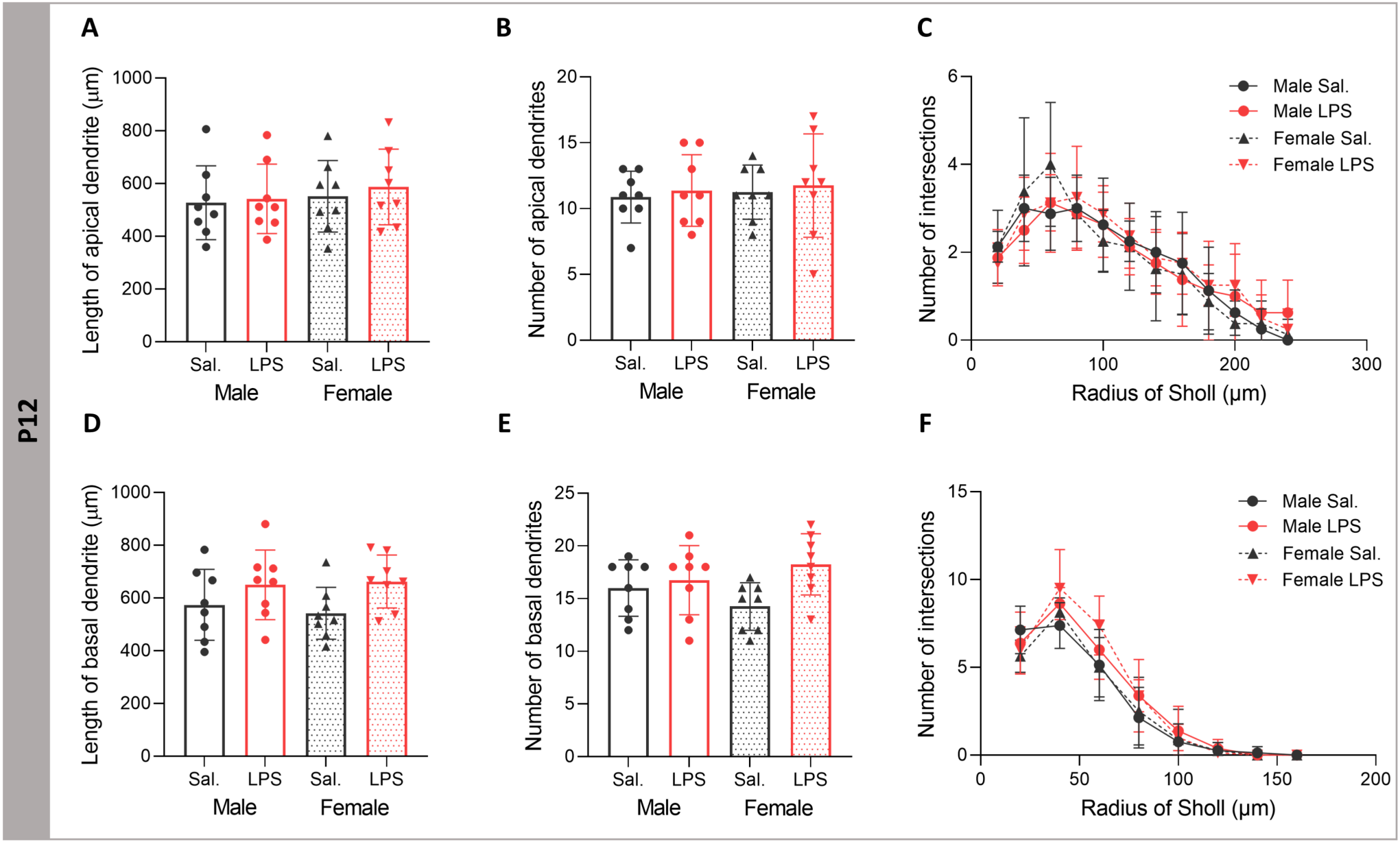
P12
A
Length of apical dendrite (µm)
1000
800
600
400
200
0
Sal.
LPS
Sal.
LPS
Male
Female
B
Number of apical dendrites
20
15
10
5
0
Sal.
LPS
Sal.
LPS
Male
Female
C
Number of intersections
6
4
2
0
0
100
200
300
Radius of Sholl (µm)
Male Sal.
Male LPS
Female Sal.
Female LPS
D
Length of basal dendrite (µm)
1000
800
600
400
200
0
Sal.
LPS
Sal.
LPS
Male
Female
E
Number of basal dendrites
25
20
15
10
5
0
Sal.
LPS
Sal.
LPS
Male
Female
F
Number of intersections
15
10
5
0
0
50
100
150
200
Radius of Sholl (µm)
Male Sal.
Male LPS
Female Sal.
Female LPS

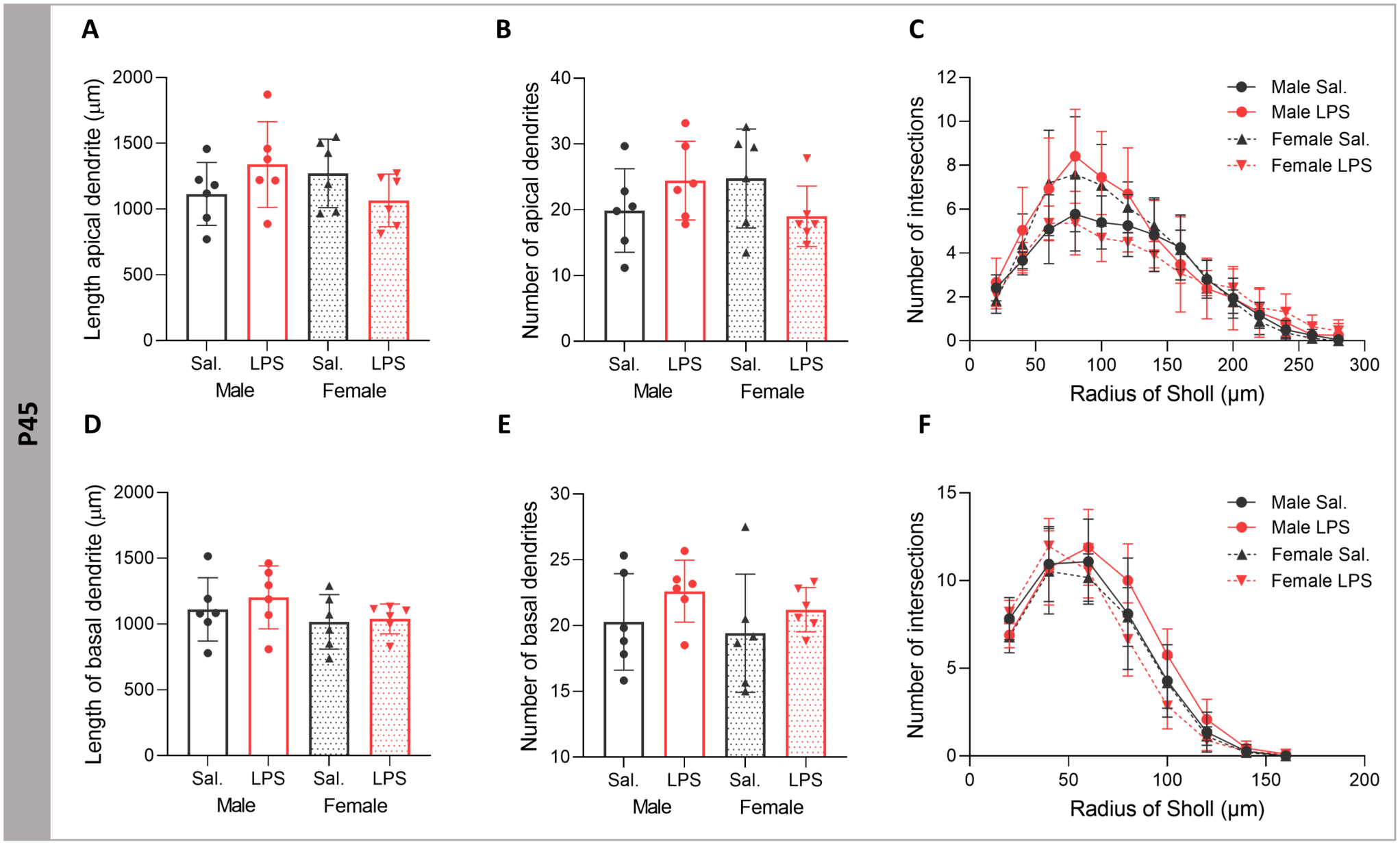
P45
A
Length apical dendrite (µm)
2000
1500
1000
500
0
Sal.
LPS
Sal.
LPS
Male
Female
B
Number of apical dendrites
40
30
20
10
0
Sal.
LPS
Sal.
LPS
Male
Female
C
Number of intersections
12
10
8
6
4
2
0
0
50
100
150
200
250
300
Radius of Sholl (µm)
Male Sal.
Male LPS
Female Sal.
Female LPS
D
Length of basal dendrite (µm)
2000
1500
1000
500
0
Sal.
LPS
Sal.
LPS
Male
Female
E
Number of basal dendrites
30
25
20
15
10
Sal.
LPS
Sal.
LPS
Male
Female
F
Number of intersections
15
10
5
0
0
50
100
150
200
Radius of Sholl (µm)
Male Sal.
Male LPS
Female Sal.
Female LPS

P45 Apical dendrite

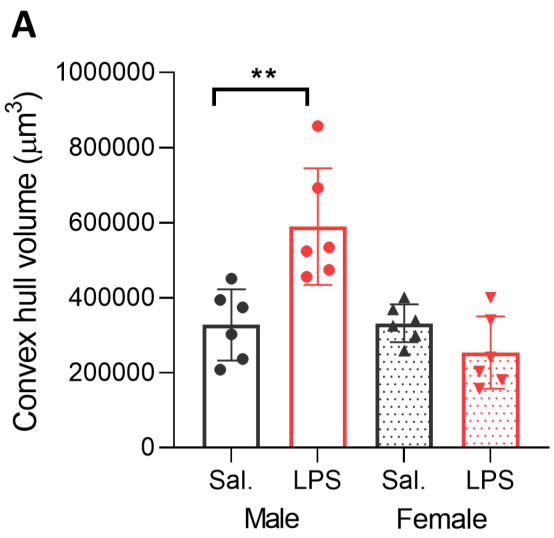

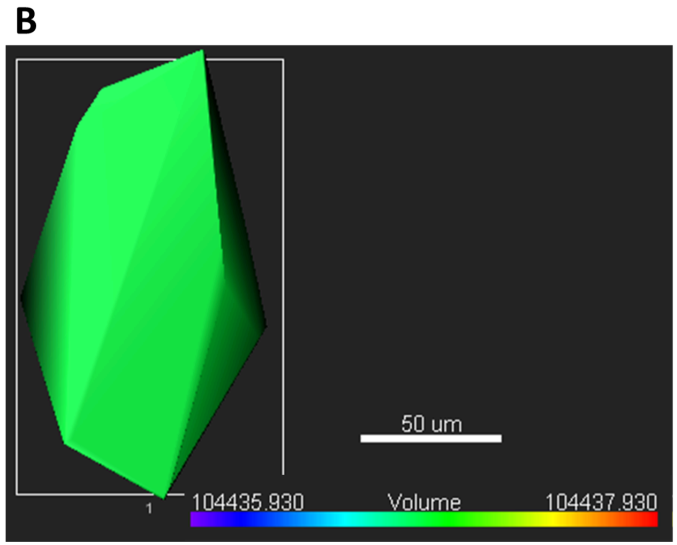

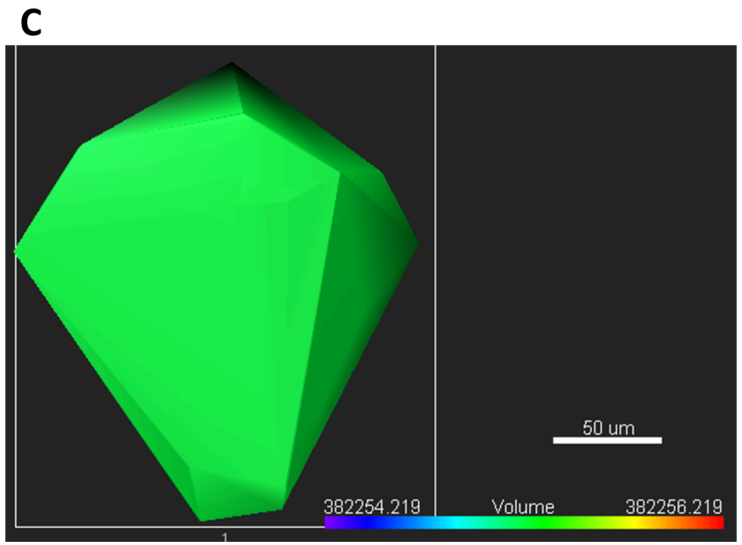

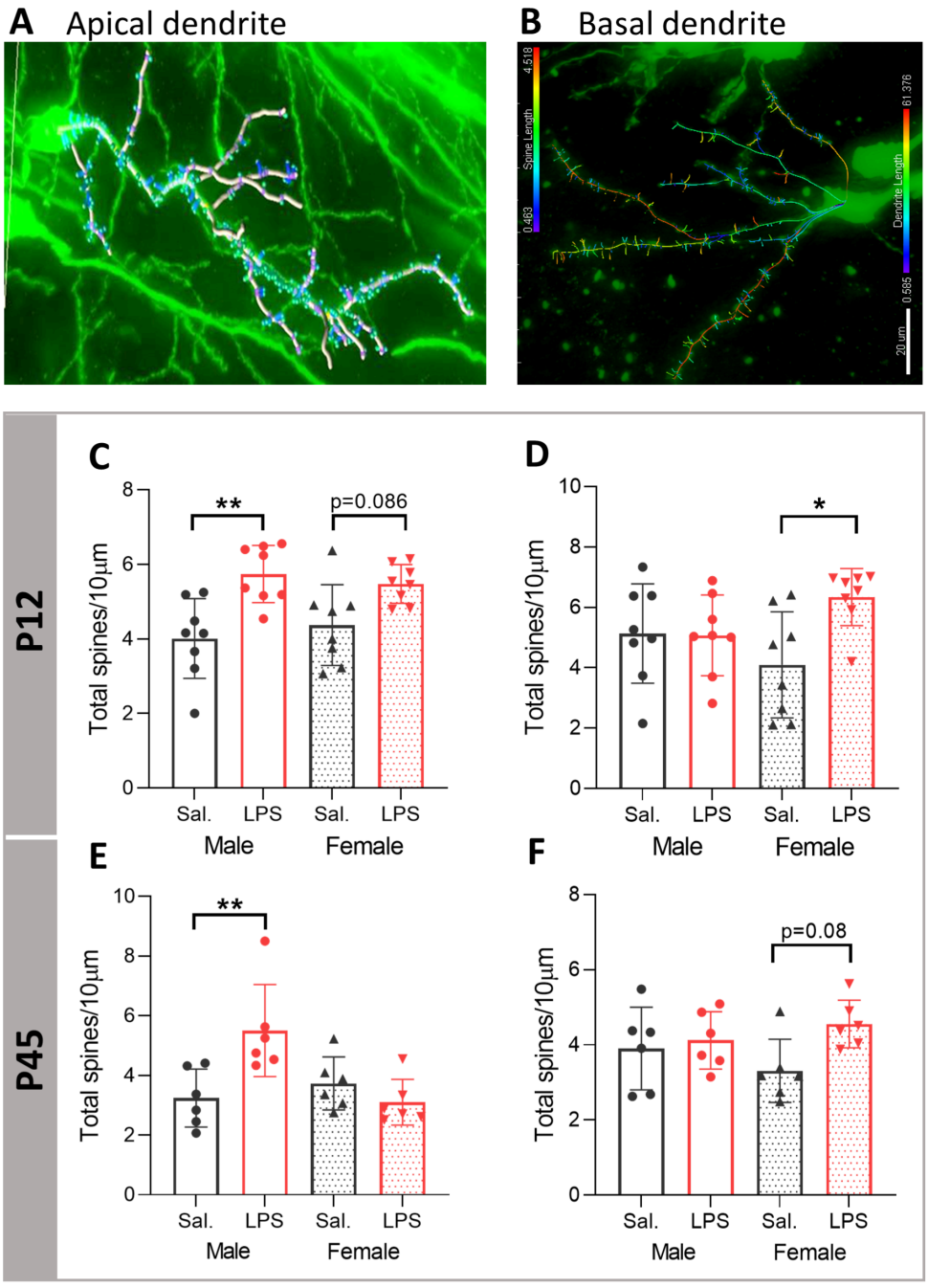
A Apical dendrite
B Basal dendrite
Spine Length
4.518
0.463
Dendrite Length
61.376
0.585
20 um
P12
P45
C
D
E
F
Total spines/10µm
Sal.
LPS
Male
Female
**
p=0.086
*
p=0.08

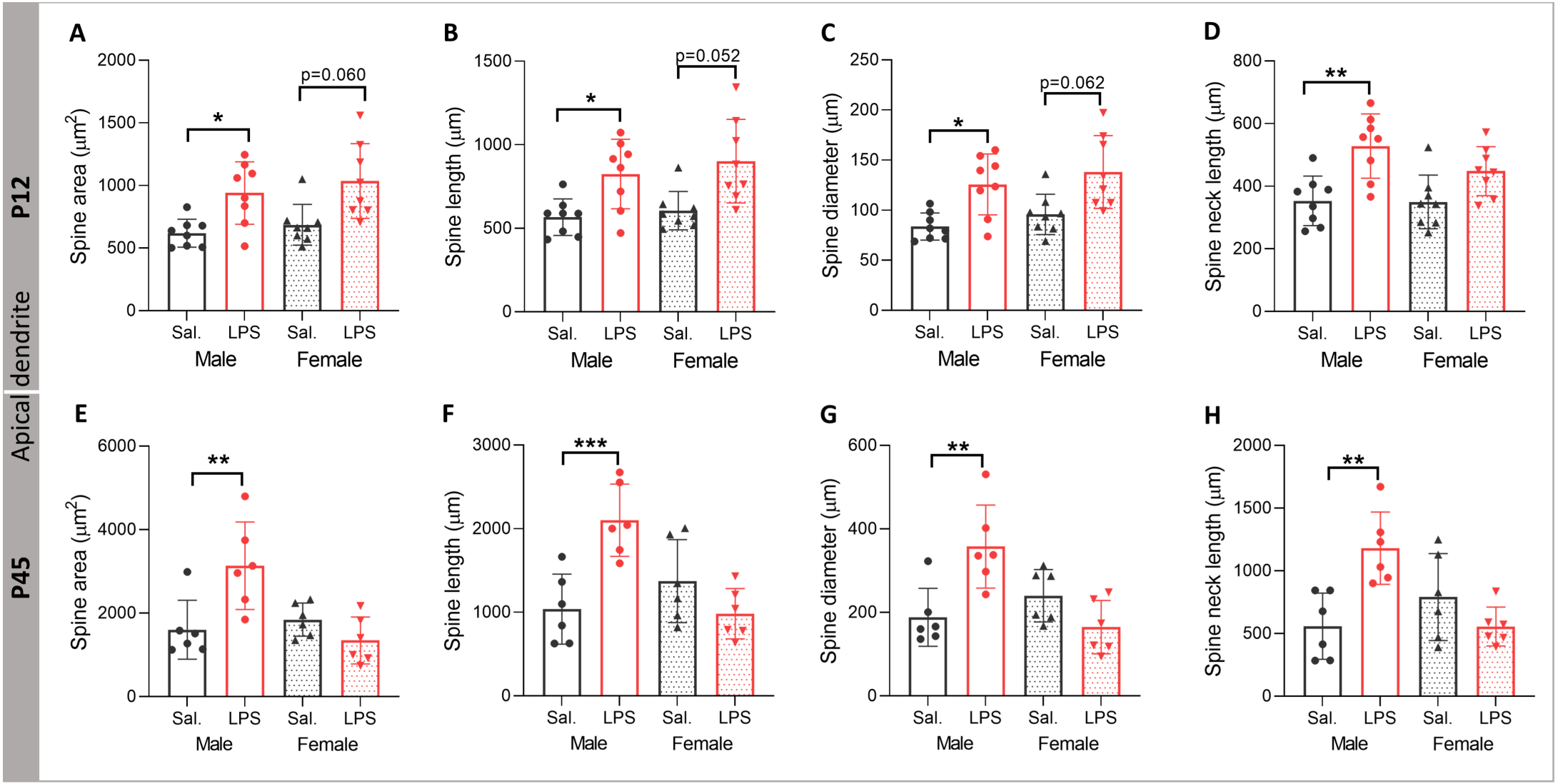
P12
Apical dendrite
P45
A
Spine area (µm²)
2000
1500
1000
500
0
*
p=0.060
Sal.
LPS
Sal.
LPS
Male
Female
B
Spine length (µm)
1500
1000
500
0
*
p=0.052
Sal.
LPS
Sal.
LPS
Male
Female
C
Spine diameter (µm)
250
200
150
100
50
0
*
p=0.062
Sal.
LPS
Sal.
LPS
Male
Female
D
Spine neck length (µm)
800
600
400
200
0
**
Sal.
LPS
Sal.
LPS
Male
Female
E
Spine area (µm²)
6000
4000
2000
0
**
Sal.
LPS
Sal.
LPS
Male
Female
F
Spine length (µm)
3000
2000
1000
0
***
Sal.
LPS
Sal.
LPS
Male
Female
G
Spine diameter (µm)
600
400
200
0
**
Sal.
LPS
Sal.
LPS
Male
Female
H
Spine neck length (µm)
2000
1500
1000
500
0
**
Sal.
LPS
Sal.
LPS
Male
Female

P12 apical dendrite

P45 apical dendrite

B Stubby

C Thin

D Mushroom

E Stubby

F Thin

G Mushroom

Total spines/10µm

Sal. LPS Sal. LPS

Male Female

p=0.096

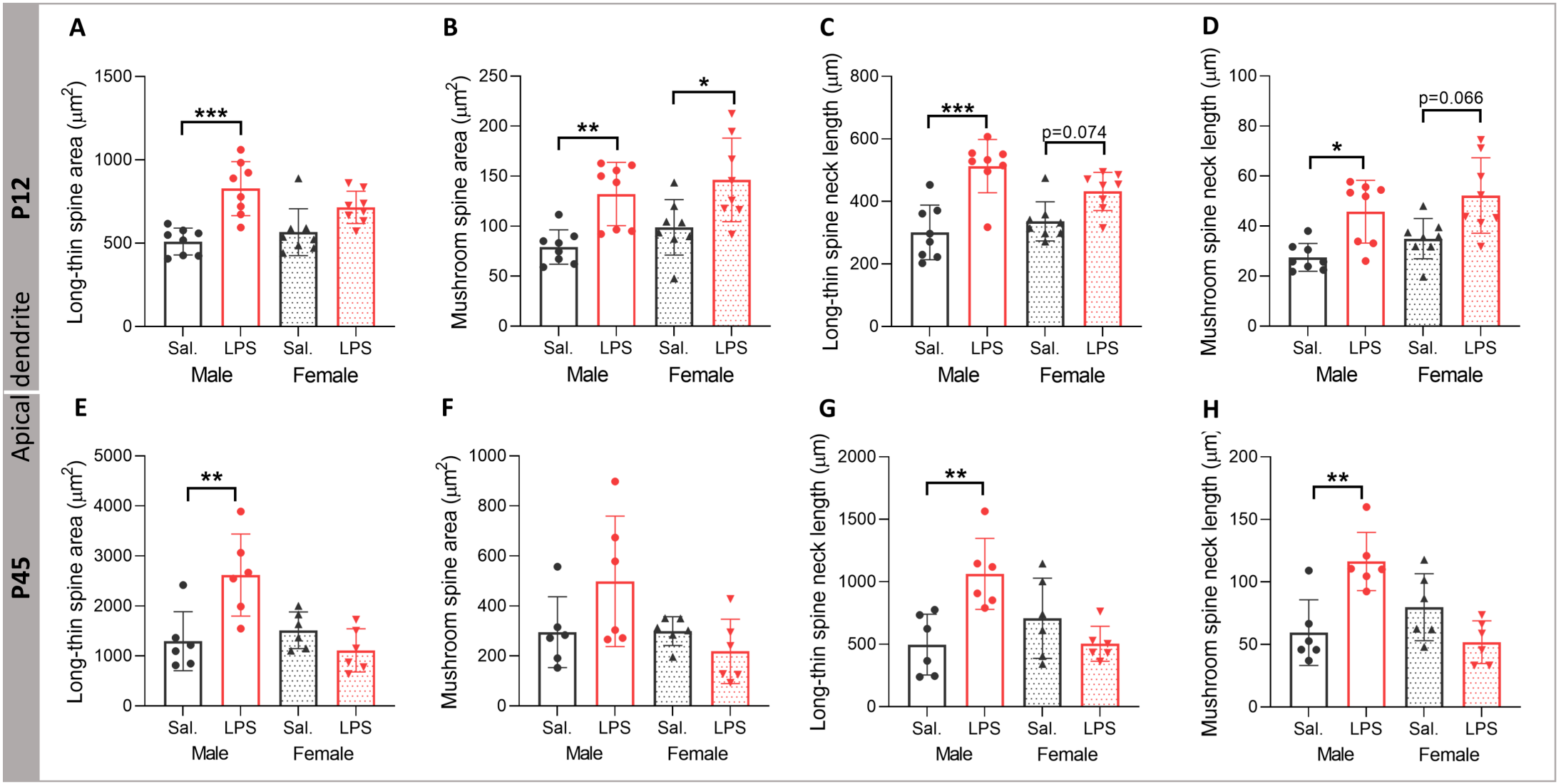
P12
Apical dendrite
P45
A
B
C
D
E
F
G
H
Long-thin spine area (μm²)
Mushroom spine area (μm²)
Long-thin spine neck length (μm)
Mushroom spine neck length (μm)
***
**
*
p=0.074
p=0.066
Sal.
LPS
Male
Female

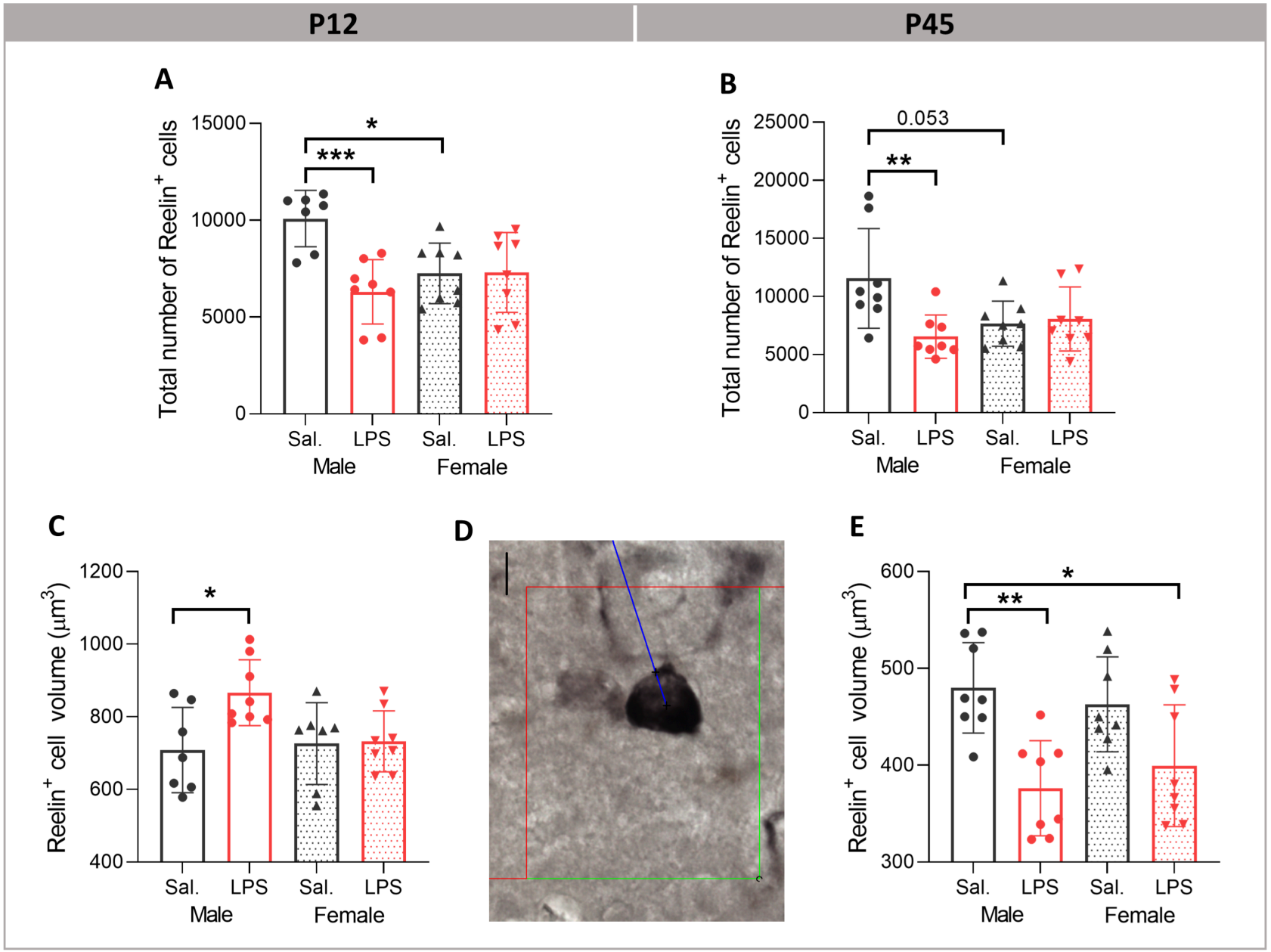
P12
P45
A
Total number of Reelin+ cells
15000
10000
5000
0
*
***
Sal.
LPS
Sal.
LPS
Male
Female
B
Total number of Reelin+ cells
25000
20000
15000
10000
5000
0
0.053
**
Sal.
LPS
Sal.
LPS
Male
Female
C
Reelin+ cell volume (µm3)
1200
1000
800
600
400
*
Sal.
LPS
Sal.
LPS
Male
Female
D
E
Reelin+ cell volume (µm3)
600
500
400
300
*
**
Sal.
LPS
Sal.
LPS
Male
Female

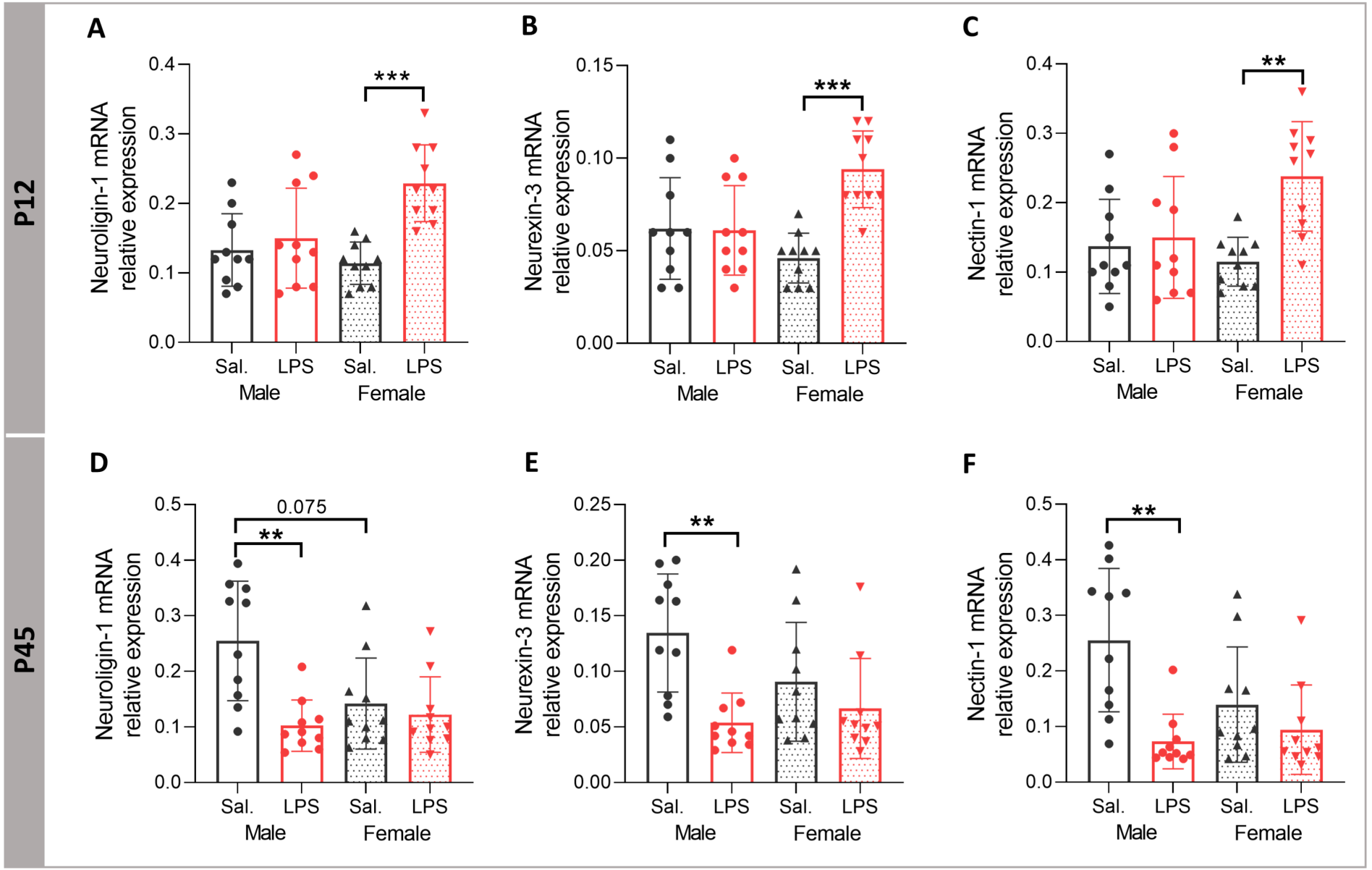
P12
P45
A
B
C
D
E
F
Neuroligin-1 mRNA relative expression
Neurexin-3 mRNA relative expression
Nectin-1 mRNA relative expression
0.0
0.1
0.2
0.3
0.4
0.00
0.05
0.10
0.15
0.20
0.25
0.5
***
**
0.075
Sal.
LPS
Male
Female

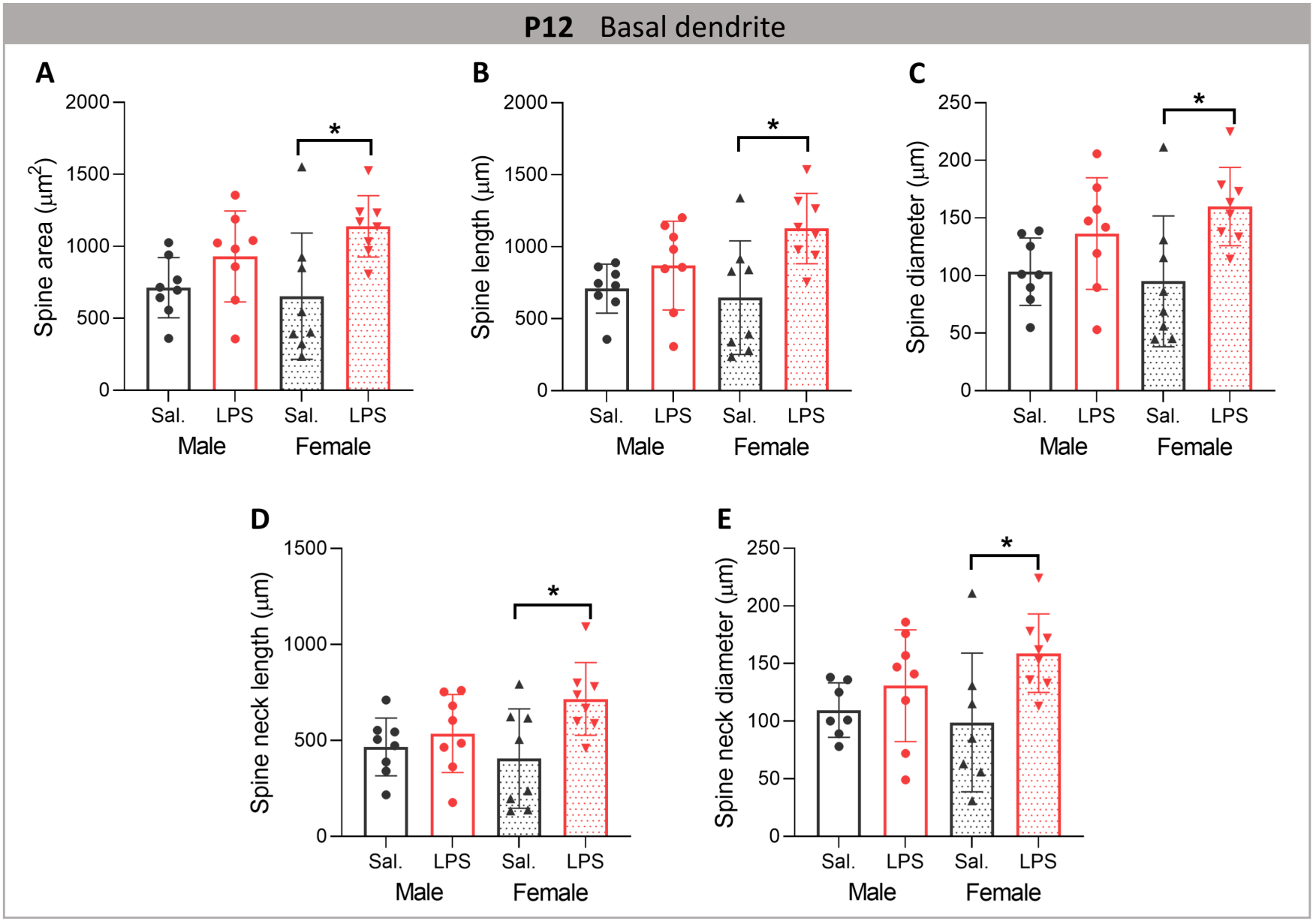
P12 Basal dendrite
A
Spine area (µm²)
2000
1500
1000
500
0
*
Sal.
LPS
Sal.
LPS
Male
Female
B
Spine length (µm)
2000
1500
1000
500
0
*
Sal.
LPS
Sal.
LPS
Male
Female
C
Spine diameter (µm)
250
200
150
100
50
0
*
Sal.
LPS
Sal.
LPS
Male
Female
D
Spine neck length (µm)
1500
1000
500
0
*
Sal.
LPS
Sal.
LPS
Male
Female
E
Spine neck diameter (µm)
250
200
150
100
50
0
*
Sal.
LPS
Sal.
LPS
Male
Female

P45 Basal dendrite

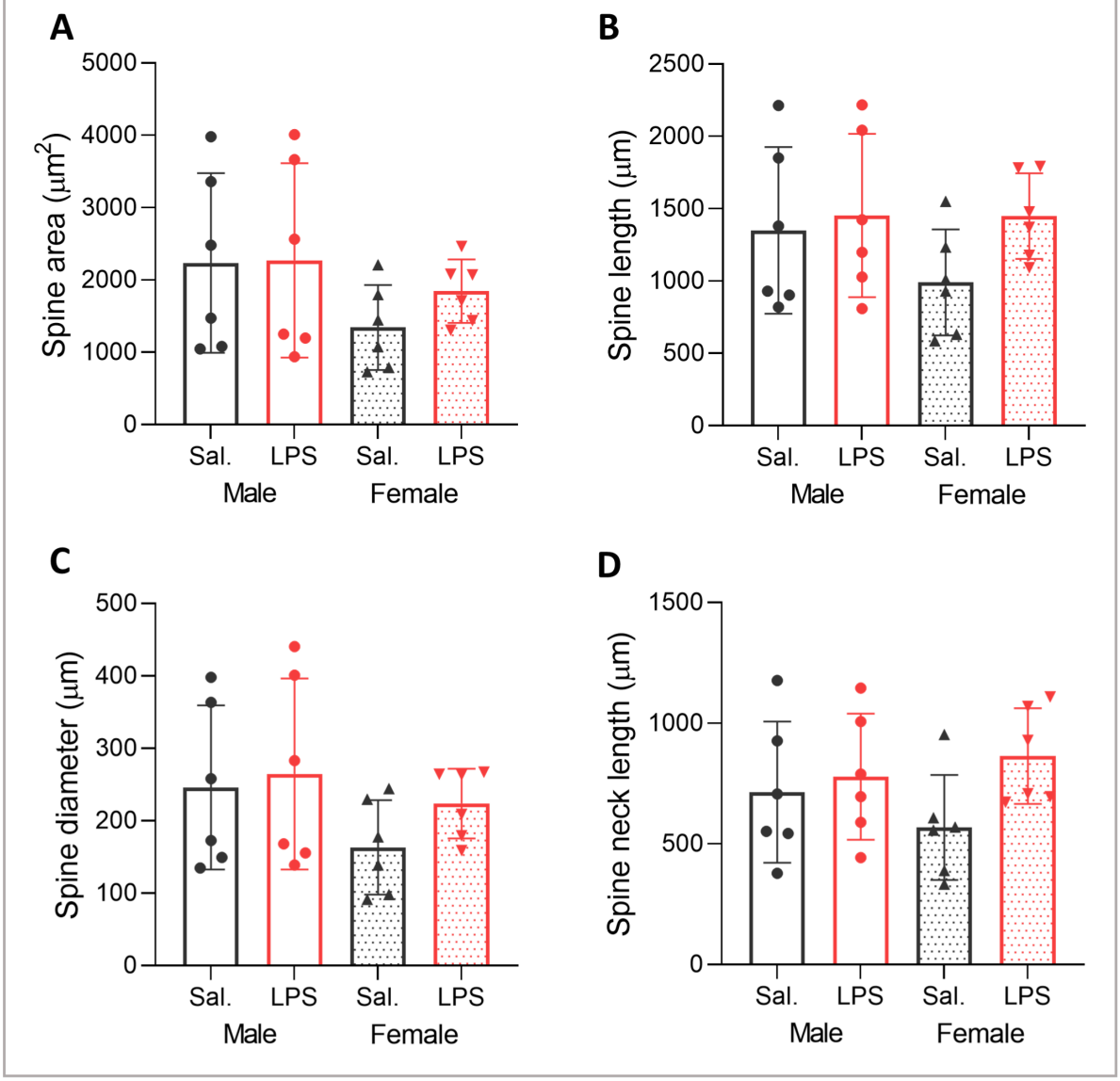

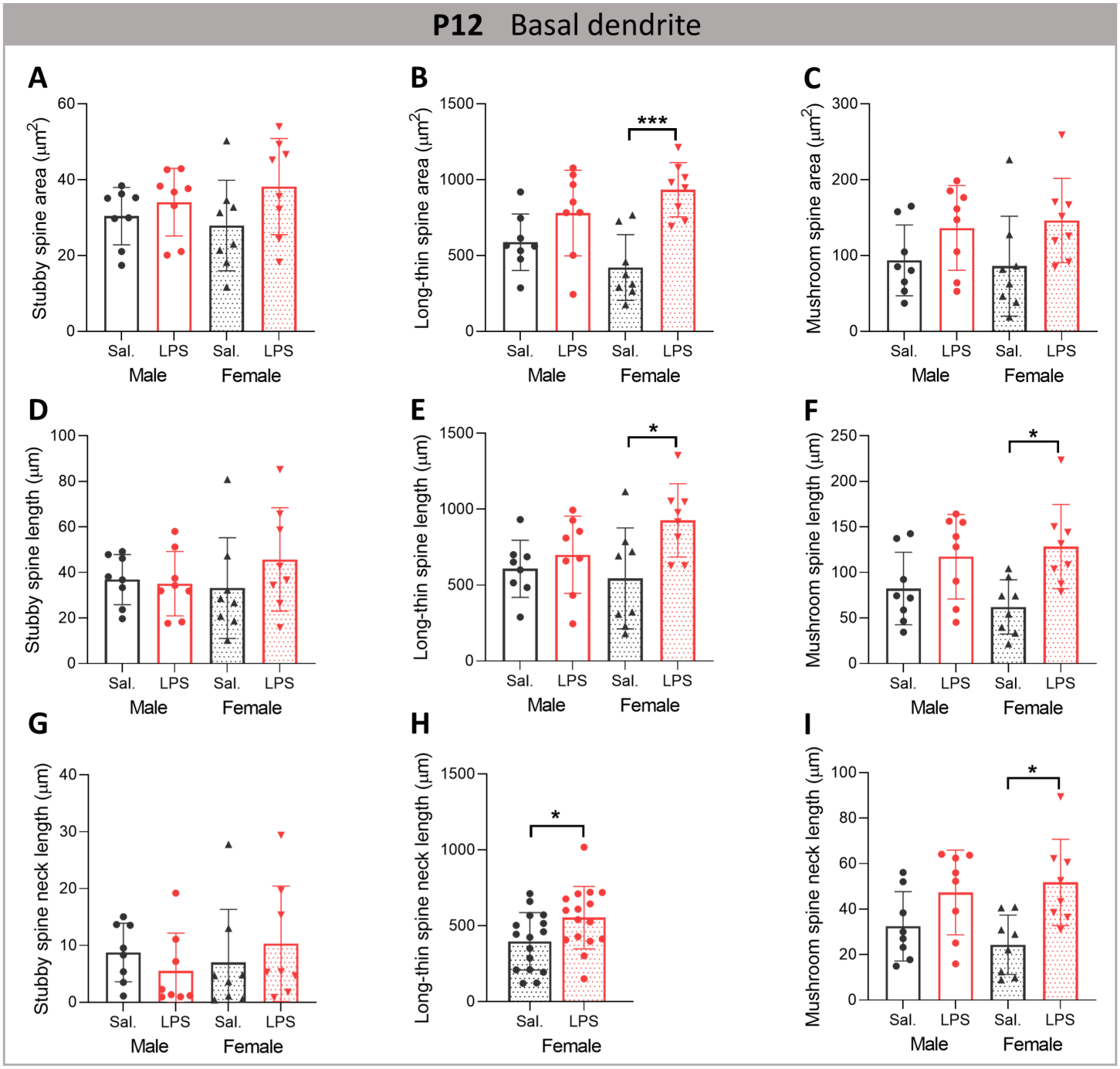
P12 Basal dendrite
A
Stubby spine area (μm2)
60
40
20
0
Sal.
LPS
Sal.
LPS
Male
Female
B
Long-thin spine area (μm2)
1500
1000
500
0
***
Sal.
LPS
Sal.
LPS
Male
Female
C
Mushroom spine area (μm2)
300
200
100
0
Sal.
LPS
Sal.
LPS
Male
Female
D
Stubby spine length (μm)
100
80
60
40
20
0
Sal.
LPS
Sal.
LPS
Male
Female
E
Long-thin spine length (μm)
1500
1000
500
0
*
Sal.
LPS
Sal.
LPS
Male
Female
F
Mushroom spine length (μm)
250
200
150
100
50
0
*
Sal.
LPS
Sal.
LPS
Male
Female
G
Stubby spine neck length (μm)
40
30
20
10
0
Sal.
LPS
Sal.
LPS
Male
Female
H
Long-thin spine neck length (μm)
1500
1000
500
0
*
Sal.
LPS
Female
I
Mushroom spine neck length (μm)
100
80
60
40
20
0
*
Sal.
LPS
Sal.
LPS
Male
Female